

# Impact of the Propulsion Modeling Approach on High-Lift Force Predictions of Propeller-Blown Wings

Cécile Casses <sup>\*</sup> and Christopher Courtin <sup>†</sup>  
*Electra.aero, Falls Church, 22042, USA*

Mark Drela <sup>‡</sup>  
*MIT Dept. of Aeronautics and Astronautics, Cambridge, MA 02139, USA*

Thomas Fitzgibbon <sup>§</sup> and Runda Ji <sup>¶</sup> and Maciej Skarysz <sup>||</sup> and Philippe Spalart <sup>\*\*</sup> and Qiqi Wang <sup>††</sup>  
*Flexcompute, Belmont, MA 02478, USA*

**Distributed electric propulsion presents new opportunities to design aircraft which take advantage of the deliberate close interaction between propellers, wings, and flaps. Significant forces and moments arise which would not be well-captured by modeling the systems in isolation. The ability to accurately predict these forces is important for a number of new vehicle designs, including electric short takeoff and landing (eSTOL) aircraft which use the interaction between the propellers and wing/flaps to generate very high wing lift coefficients, if normalized by the flight speed. The flow field at the propellers is strongly influenced by the presence of the wing, and vice versa.**

**This paper presents CFD analyses relevant to an eSTOL wing in a high-lift configuration, comparing four different approaches to modeling the propellers - an actuator disk, a steady and an unsteady blade element model, and a blade-resolved unsteady simulation. This is done in the Flow360 Navier-Stokes solver developed by Flexcompute. We begin with an isolated rotor, continue with a model problem that comprises a single rotor with behind it a section of wing and flap, and conclude with a full 3D configuration. The actuator disk is advantageous from a computational time point of view, but introduces error into the solutions because it cannot adapt to strongly varying local inflow conditions. The time-resolved simulations are expected to give the most accurate solutions, but are computationally expensive. An adaptive blade-element model gives a good compromise between accuracy and performance.**

## I. Nomenclature

$\alpha$	=	Angle of Attack
$AR$	=	Aspect Ratio
$\beta$	=	Local Blade Twist Angle
$c$	=	Blade or Wing Chord
$c_{bl}$	=	Blade Line Chord
$C_D$	=	Drag Coefficient $D/(0.5 \rho_\infty V^2 S_{ref})$
$C_{f_x}$	=	Skin Friction Coefficient
$C_L$	=	Lift Coefficient $L/(0.5 \rho_\infty V^2 S_{ref})$
$C_p$	=	Pressure Coefficient
$C_{p_t}$	=	Total Pressure Coefficient

---

<sup>\*</sup>Senior Flight Physics Engineer, AIAA Member

<sup>†</sup>Flight Physics Lead Engineer, AIAA Member

<sup>‡</sup>Terry J. Kohler Professor, AIAA Fellow

<sup>§</sup>CFD Research Scientist, AIAA Senior Member

<sup>¶</sup>CFD Application Scientist, AIAA Member

<sup>||</sup>Product Manager

<sup>\*\*</sup>Director of Flow Physics, AIAA Senior Member and Associate Technical Fellow

<sup>††</sup>Co-founder, AIAA Associate Fellow

$C_M$	=	Moment Coefficient $M/(0.5 \rho_\infty V^2 S_{\text{ref}} c)$
$C_Q$	=	Torque Coefficient $Q/(0.5 \rho_\infty (\Omega R)^2 \pi R^3)$
$C_T$	=	Thrust Coefficient $T/(0.5 \rho_\infty (\Omega R)^2 \pi R^2)$
$f_{\text{ax}}$	=	Axial force per unit area
$f_{\text{cir}}$	=	Circumferential force per unit area
$F_{\text{ax}}$	=	Axial force per unit volume
$F_{\text{cir}}$	=	Circumferential force per unit volume
$\lambda$	=	Propeller Advance Ratio
$\Omega$	=	Rotor Angular Speed, rad/sec
$\phi$	=	Local Disk Flow Angle
$R$	=	Blade Radius
$\rho$	=	Density
$\sigma$	=	Local Solidity
$S_{\text{ref}}$	=	Reference Surface Area
$t$	=	Thickness of BET Disk
$T_c$	=	Thrust Coefficient $T/(0.5 \rho_\infty V^2 S_{\text{ref}})$
$V_\infty$	=	Freestream Velocity

## II. Introduction

Distributed electric propulsion makes it practical to design aircraft which take advantage of wide-spread aeropropulsive interactions. One example of these types of vehicles is eSTOL aircraft, which use the deflection of the propeller slipstream by the wing and trailing edge flaps to increase the effective wing lift coefficient, enabling low flight speeds and short takeoff and landing distances.

The design of these types of aircraft presents a new challenge, as they introduce a large number of configuration design variables such as motor count, size, and position, as well as flap type, size and angle, that strongly impact the performance of the vehicle and for which there is little existing design guidance. In addition, it is not obvious that relatively conventional multi-element high lift systems are optimal for blown-lift applications, since the blowing energizes the element boundary layers and wakes and also changes the surface pressure distributions relative to unblown high lift flows. All this makes eSTOL aircraft a compelling case for early high-fidelity computational fluid dynamics (CFD) simulation, in order to understand the competing trades and explore the complex design space with adequate physical modeling fidelity.

One of the challenges with using high fidelity CFD in design development is the time, effort, and computational cost required to generate, mesh and analyze many different flight conditions and design variations. This, and the fact that the eSTOL design space to be explored is large, motivates finding modelling approaches which offer a good balance between high modeling fidelity with low computational cost.

For blown-lift configurations, the type of propeller model chosen is especially important. Because of the close proximity of the propeller to the wing, the local flow field at the propeller is significantly impacted by the presence of the wing. In order to establish which approach is best in industrial practice, four propeller models are compared: 1) an actuator disk (AD) with specified jumps in streamwise and tangential velocity [1, 2], 2) a blade-element model [3–6] (BET disk) run in a steady circumferentially-averaged form, 3) an unsteady BET line model, and 4) a time-resolved simulation of the full propeller geometry.

These models are compared in three cases as show in Figure 1; a single propeller in isolation, a single propeller-wing combination, and multiple propellers arranged on the aircraft wing. The single propeller in isolation provides a baseline comparison of the different propulsion models, while the single propeller-wing combination approximates a 2D blown-lift interaction. This case is subsequently referred to as the single-rotor model problem. The full aircraft geometry case includes 3D effects that arise from a finite wing and shows how the models compare in a realistic design case.

For the cases where a wing is present, a high lift landing case with 60 degrees of flap deflection is analyzed. This case features significant distortion of the local flow at the propellers, which makes the commonly used actuator disk model with a fixed pressure and tangential velocity jumps very suspect, while the other higher-fidelity models are more likely to produce more reasonable results.

Section III below describes the approach taken to setting up the analysis for these problems, including geometry generation and grid refinement. The four propulsion models were then compared for the isolated propeller case (Section V.A) and the model problem case (Section V.B). The model problem case is also used to investigate the effects



of including the propeller pylon and centerbody (Section V.B.1). Finally, the actuator disk and steady and unsteady blade element models are compared on the 3D aircraft geometry (Section V.C).

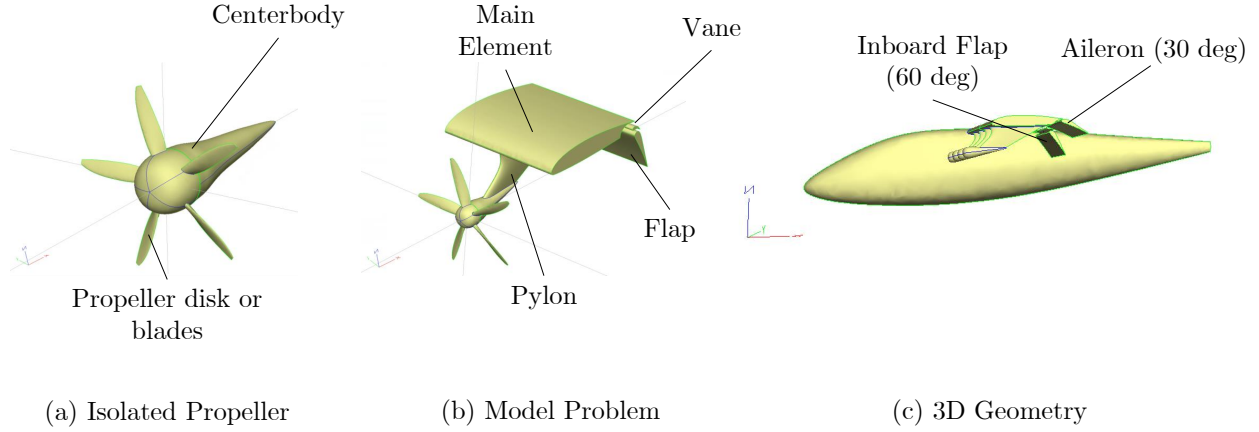


**Fig. 1** Comparison of the different geometries, with labels showing the primary features discussed in subsequent sections.

### III. CFD Approach

#### A. Geometry & Mesh Generation

The geometry used for this aircraft is representative of an eSTOL aircraft in the landing configuration, which features a 60 deg double-slotted Fowler flap. To enable rapid generation of different analysis cases and meshes, the geometries studied in this paper are defined in a parametric way using Engineering Sketch Pad (ESP) [7]. Figure 2 shows how this tool uses airfoil section definitions and fuselage cross-sections to build up the test cases of interest.

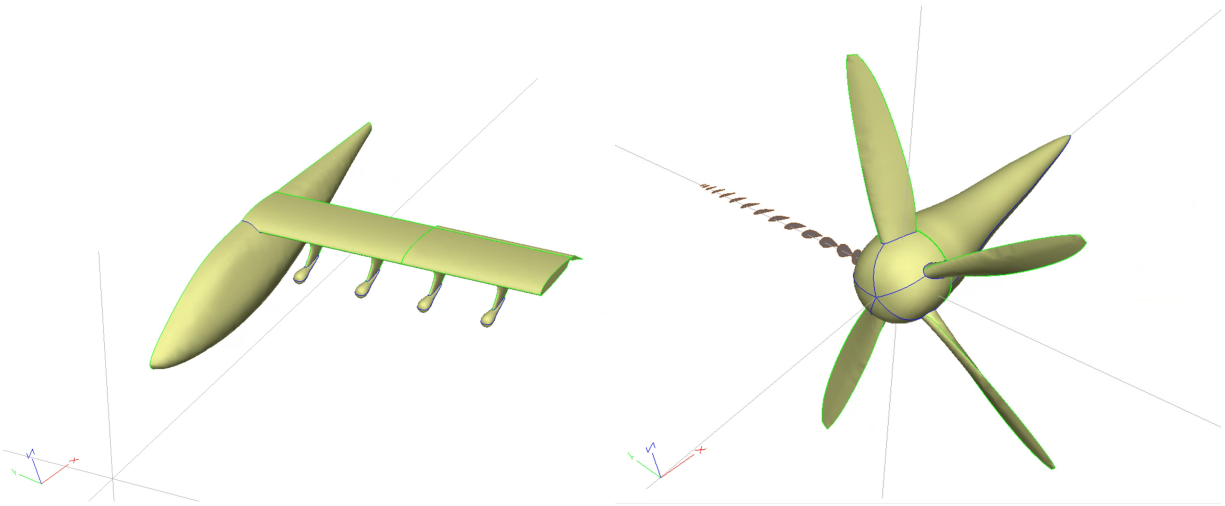


**Fig. 2** Left: Parameterized airplane constructed in ESP. Right: Parameterized rotor constructed from airfoil cross-sections.

Critically, a surface mesh with local refinement on leading and trailing edges is also generated parametrically, with the mesh refinement parameters specified alongside the geometry definition (by tagging those edges or faces); an example can be seen in Fig. 3.

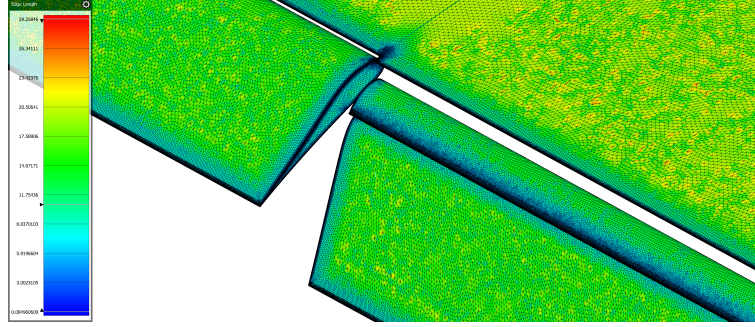


**Fig. 3 Local surface mesh refinement on the main-element, vane, flap and aileron.**

The meshing configuration file also contains information about dimensions, position and orientation of propulsor disks as well as sources, i.e., volume refinement zones. For the full aircraft configuration, this can be seen in the left side of Fig. 4 coloured green and orange, respectively. The right side shows those refinement zones as the high-density rectangular area.

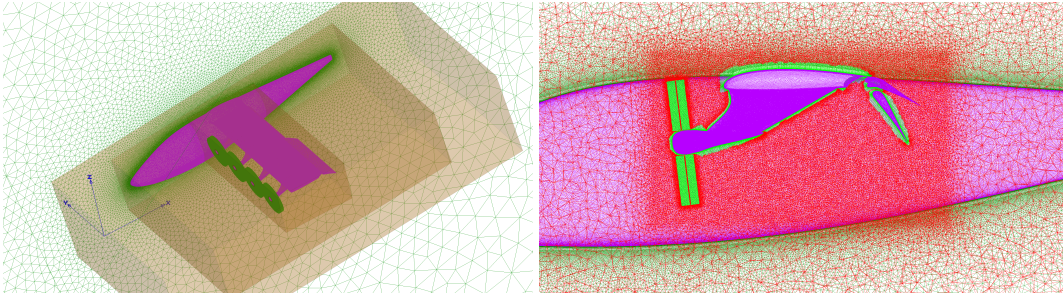


**Fig. 4 An overview of surface meshes (pink), actuator disks (green) and grid refinement regions (orange) is shown at left, with a cross-section detail of the flaps shown at right.**

This automatic co-generation of parametric geometries and meshes is key to enabling rapid design iteration and analysis.

## **B. Model Geometry Comparison**

This paper focuses on the complex interaction of the propeller flow with the wing and high lift device. In order to validate our modelling, we first consider an isolated propeller, then a model problem comprised of a single-rotor, wing, and high lift device, and lastly we looked at the full 3D geometry. The geometries are displayed in Fig. 1, and the major features of each case are labeled. The isolated propeller case consists of a modeled centerbody and propeller blades. The model problem adds a pylon and a three-element wing, which is comprised of a main element, a flap, and a fixed vane above the flap. The flap and vane operate as a double-slotted Fowler flap. The full aircraft geometry adds a fuselage and a single-slotted aileron on the outboard section, deflected to 30 degrees. Each geometry was run in CFD using four different propulsion models. Those models are the Actuator Disk (AD), the Steady Blade Element Model (BET disk), the Unsteady Blade Element Model (BET line), and a full unsteady simulation. The mathematical description of those models is added in App. VII.A.

## **IV. Problem Setup and Grid Refinement**

This section describes in more details the geometry for each problem and its associated mesh.

### **A. Isolated Propeller**

First an isolated propeller and its centerbody is considered. It is a five-blade propeller with a solidity of 0.24. The geometry is shown in Fig. 1, (a).

A speed sweep is performed to vary the advance ratio,  $\lambda = V_\infty / (\Omega R)$ , from 0.03 to 0.25 at a fixed RPM of 4000, the highest speed. Mach effects are negligible for the maximum power conditions. The effect of angle of attack is also examined by varying angle of attack from 0 to 10 deg.

Both a disk density study and a disk thickness study are performed to be able to compare the four different propulsion models. Those studies are based on the hardest flow condition that is expected to be seen, which is the lowest freestream velocity. Grid density results can be found in App. VII.B.1. Precautions have been taken to refine both the disk around the propeller anisotropically and the different volume mesh cylinders isotropically to get four meshes from coarse to extra fine. The main takeaway is that volume disk thickness and solver disk thickness are the main contributors to convergence so the disk thickness study is shown in the next section.

### 1. Disk Thickness Study

One disk thickness study was done for the actuator disk, BET disk or BET line. The meshing parameters are found in Tab. 1. Two meshes were considered so that when the disk thickness is varied there is enough layers across the disk. At the same time the region where the body force is added is always fully enclosed by the anisotropic refinement region in the mesh, i.e. the solver disk thickness is less or equal to the volume mesh disk thickness.

**Table 1 Disk thickness study for actuator disk.**

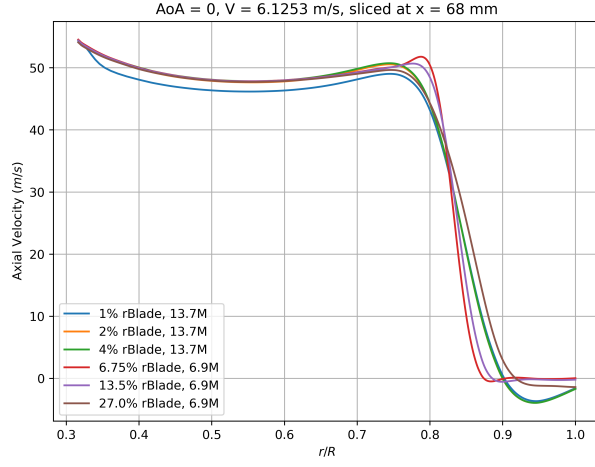
	Resolution	Medium	Medium
	Total number of nodes	13.7M	6.9M
Surface	Max edge length	9	9
	Curvature resolution angle	12	12
Volume	Spacing in refinement region 1	18	18
	Spacing in refinement region 2	36	36
	Spacing in refinement region 3	72	72
	Spacing in refinement region 4	144	144
	Disk thickness in % of $R$	4%	27%
	nCell <sub>thickness</sub>	40	40
	nCell <sub>radial</sub>	200	200
	nCell <sub>circumferential</sub>	1000	1000
	Growth rate	1.2	1.2
Solver	Disk thickness in % of $R$	1%, 2%, 4%	6.75%, 13.5%, 27%

The results of the disk thickness study are found in Fig. 5. It compares axial velocity and swirl versus blade station. Swirl is computed by rotating (and translating in 3D cases) the position and velocity vectors in to match the orientation of the rotor disk axis. In this case, a rotation about the y axis of 7 degrees is performed. Then the following equation is used to compute the swirl:

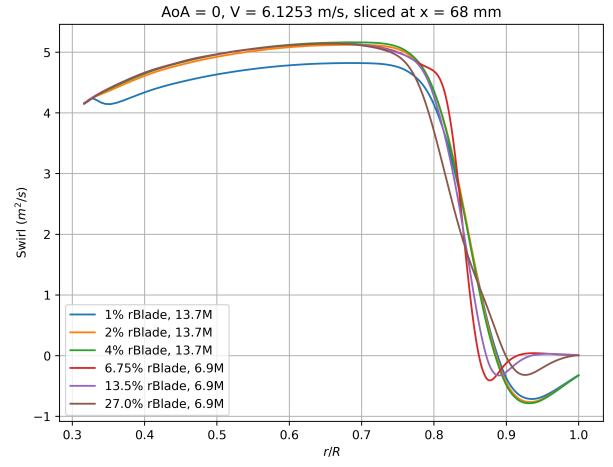
$$\text{swirl} = V_y z - V_z y \quad (1)$$

Minimal variation is seen for the different disk thicknesses for the actuator disk (a) and BET disk (c), the smallest disk thickness indicates smaller swirl level (b). In (d), the increase in swirl from the unsteady run (corresponding to blade tip separation described in Sec. V.A) is only modelled by the 27% $R$  disk thickness mesh with a solver disk thickness of 6.75% or 13.5% $R$ . Disk thickness of 27% $R$  is actually too thick, as shown in equations 2 and 3, the volume force is distributed in such a thick region and hence the force per unit volume is too low. For BET line, (e), and (f), the disk thickness has more impact on axial velocity and swirl with 13.5% $R$  being the closest.

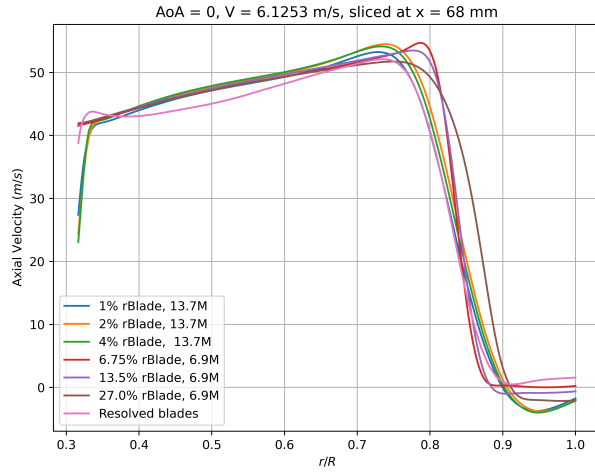
All subsequent results of isolated propeller were obtained using the 27% $R$  disk thickness mesh with 13.5% $R$  solver disk thickness. The unsteady results were obtained from a fine mesh, more details is in App. VII.B.1.



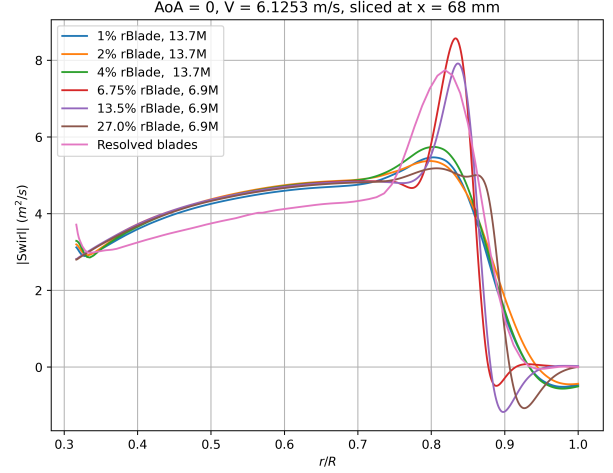
(a) AD, Axial Velocity



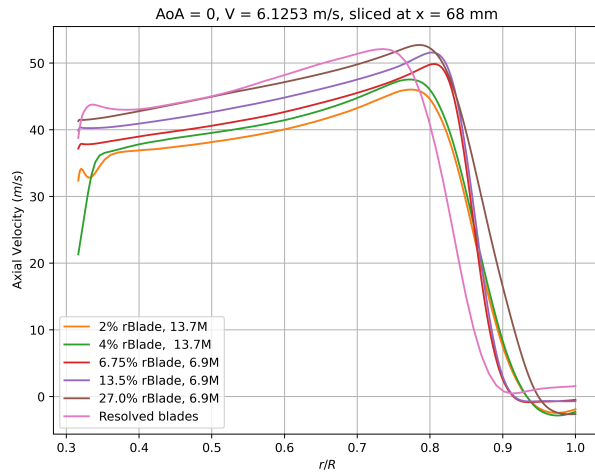
(b) AD, Swirl



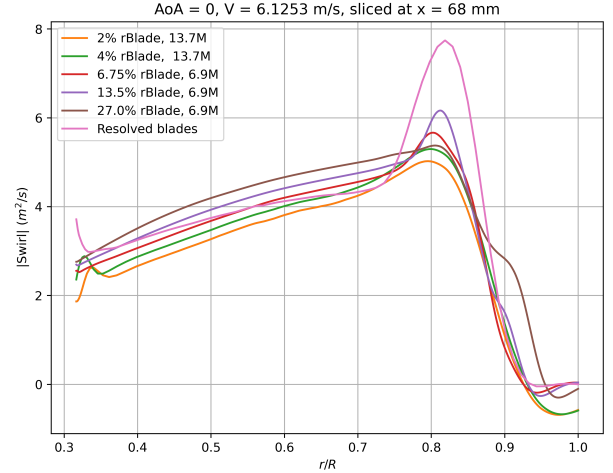
(c) BET Disk, Axial Velocity



(d) BET Disk, Swirl



(e) BET Line, Axial Velocity



(f) BET Line, Swirl

**Fig. 5 Comparison of axial velocity and swirl extracted from a downstream wake with different solver disk thickness for  $V_\infty = 6.12$  m/s. (a), (b) Actuator Disk, (c), (d) BET Disk, and (e), (f) BET line.**

## B. Single-Rotor Model Problem

The primary physical/numerical challenge in simulating the Electra airplane is to model at a reasonable cost large tractor rotors attached to a wing with high-lift devices and a high lift coefficient, especially since it is based on the flight velocity. This introduces a strong distortion of the flow, with serious consequences in terms of rotor performance, control, and blade fatigue. These phenomena can be studied at much lower cost and with better clarity than with a full configuration using the following model problem.

The wing has essentially no sweep, with a fairly high aspect ratio and number of rotors, so that a section of the wing with only one rotor is fairly representative of the entire wing. Double-slotted flaps are used to achieve high jet deflection and thus high lift coefficient. The model wing has a constant chord and a geometry taken directly from the 3D configuration, and the lateral boundary conditions are symmetry planes. This mimics the 3D wing situation where adjacent propellers rotate in opposite directions and hence are mirror images about the computational boundary planes. With a very large number of propellers in 3D, the symmetry would apply to the time-average flow, but not exactly to the time-dependent flow.

The centerbody used in the isolated propeller cases as well as a pylon are added to look at the effect of those components on swirl and performance. Figure 1 (b) shows the geometry with flap angle of 60 degrees, representative of a landing condition, and its parameters are given in Table 2. For those cases, the propeller was scaled in xRotor [8] by a factor of 1.6 while keeping the same centerbody. This was done to match the propeller to this wing geometry. The propeller is rotating clockwise from the pilot's view. All cases were run at 15.433 m/s (30 knots) which is the touchdown speed expected for those eSTOL vehicles.

The objective is to compare predictions from the lowest fidelity (cheapest) to the highest fidelity (most expensive) rotor representations. The best accuracy/cost compromise will then be considered for full 3D simulations.

The model problem has an effectively infinite aspect ratio, due to its symmetry endplanes. To correctly represent a 3D wing, the model's specified freestream angle of attack must therefore be reduced to account for the wing trailing vortex system's downwash angle, which for the present configurations is very high. We invoked elliptically-loaded lifting-line theory, by which the tangent of the downwash angle is  $C_L/\pi AR$ , but this gives excessive values and it was discarded (recall that lifting-line theory assumes that  $C_L/AR \ll 1$ ). There are also end effects when the full configuration has only two rotors side-by-side, flanked by the body on the inboard side and a smaller flap on the outboard side. Instead, we compared the model flow fields to the 3D geometry and made sure the flow behavior was similar. The model cases were run without a vortex term in the far-field boundary condition, but the domain was very large. In any case, the purpose is not a very close correspondence with the 3D flow, and the angle of attack and boundary condition were the same for the different propulsion models.

**Table 2 Model-problem geometry parameters.**

Span/Chord	0.665
Propeller Radius/Chord	0.314
Vane/Flap Deflection (deg)	60

A grid density study was performed for the BET models and the disk thickness was used from the isolated propeller study. Details are given in App. VII.B.2. Variation in thrust, torque, and airframe  $C_L$ ,  $C_D$ , and  $C_M$  were negligible across the three meshes so the coarser grid was chosen. This grid was used for all propulsion models.

## C. 3D Geometry

A half-aircraft geometry is run to compare the results to the model problem. Figure 1 (c) shows the geometry and the parameters are listed in Table 3.

The same wing and double-slotted flap airfoils, propellers, centerbodies and pylons as the model problem are used. The aspect ratio is 6.4. The left outboard propeller is called propeller 1 and is located in front of the aileron, while the right inboard propeller is called propeller 4 and is located in front of the flap. The propellers are located  $0.20c$  forward of the wing leading edge and  $0.23c$  down the wing leading edge. Adjacent propellers have opposite rotation direction. Propeller 4 is rotating clockwise from the pilot's view. The flap break is located at 54.7% of the half span so that two propellers blow the flap and two propellers blow the aileron.

**Table 3 3D geometry parameters.**

Span/chord	6.424
Propeller Radius/chord	0.314
Number of propellers	4 per half-span
Vane/Flap Deflection (deg)	60
Aileron Deflection (deg)	30

Because there was not a lot of variation in performance from the model problem grid density study, the same mesh parameters were applied to the 3D geometry.

## V. Results

Now that each problem has been defined, the results are shown.

### A. Isolated Propeller

Sweep conditions are summarized in Tab. 4. Regarding convergence, the residual tolerances were set to  $1e-10$  for the flow residual and  $1e-8$  for the turbulence residuals. The majority of simulations converged in under 5,000 iterations for the AD and BET Disk cases. For the BET line simulations, initially 5 revolutions were performed, showing good convergence of the BET forces. For lower inflow speeds (6.12 - 14.97 m/s), an additional 5 revolutions were simulated to wash the wake further downstream and converge the loads on the centerbody. In general, the hardest cases to converge, were the cases with low inflow speeds. The chosen disk thickness was also driven by convergence properties as low disk thickness values led to stagnation of the steady residuals at  $1e-7$  and in some cases divergence of the solver.

**Table 4 Isolated Propeller Flow Conditions.**

$\alpha$ (deg)	[0, 10]
RPM	4000
$V_\infty$ (m/s)	[6.12, 9.53, 14.97, 20.08, 28.58, 47.64]
$\lambda$	[0.032, 0.050, 0.079, 0.105, 0.150, 0.184, 0.250]

Integrated thrust, torque, and power are compared for the various propulsion models and different angles of attack in Fig. 6. We first observe that angle of attack has almost no impact on the integrated results. When comparing to the full unsteady treatment, the BET line is really close in thrust with a 5% difference at the very low speeds where tip vortices are observed due to tip separation, while in torque there is a 3% - 7% offset, increasing with decreasing airspeed. Actuator disk and BET disk are further away both in terms of thrust (16% at the low speeds, 25% at the highest speed) and torque (10% at the low speeds, 23% at the highest speed). Note that the actuator disk input distributions are chosen by the user (such that a target thrust is obtained) so that it is not surprising that thrust is closer but torque is not as good.

Those results can be explained when looking at axial velocity and swirl distributions versus blade station,  $r/R$ , in Fig. 7. At 9.5 m/s, graphs (a) and (b), the unsteady simulation shows a big increase in swirl around  $r/R = 0.85$  which is predicted by the BET models; however, the BET disk overpredicts the swirl inboard. The actuator disk simulation does not show any increase. In terms of axial velocity, the actuator disk overpredicts it inboard of the blade, BET line giving the best match. As speed increases, BET line becomes closer to unsteady both for axial velocity and swirl. BET disk overpredicts both slightly. Sectional thrust and torque distributions are also shown in Fig. 8. Those plots are a confirmation that BET line is closer to unsteady, although both BET models predicts the shape of the curves well.

Swirl contours are added for two velocities in Fig. 9, and 10. At the low speeds, the unsteady simulation shows a high magnitude of swirl as the tip vortices shed and mix along the axial direction. The BET line captures some of that effect. In the BET disk, the swirl increase is briefly noticed at the tip of the first blade passing while the actuator disk does not show any. At the highest velocity, the swirl intensity decreases but the unsteady and BET line models show higher swirl at each blade passing. It is interesting to note that for the unsteady simulations lower speeds, there is an upstream swirl impact due to the bound vortex of the blade causing circumferential velocity upstream of the rotor. The

swirl is based on the angular velocity, but better reflects angular momentum; note that in the flow of a line vortex, the swirl is independent of radius. It drops to zero outside the streamtube of the rotor.

The last visualizations show a Q-criterion plot to better visualize those tip vortices shedding and mixing. Figures 11, and 12 (a) and (b) shows a shear layer that continues downstream while (c) and (d) shows the tip vortices. Remarks about the Q-criterion are in order. First it was created to display vortices, and exclude smooth shear layers. This is why it does not display the wake's boundary for the steady models, in Fig. 11 (a), (b). Vorticity isosurfaces would mark the "sleeve". The early part of the shear layer is marked by the Q-criterion because of its curvature. Second, Fig. 11c gives the appearance that the tip vortices end, which is of course not possible. The reason is that the vortices are slowly being diffused, so that even the peak value of Q falls below the level which the user chose. The helices actually continue. Fig. 11d shows regions with Q above the threshold much further along, presumably because the peak Q level starts higher than with the BET line approach, and also the "more turbulent" character of the flow introduces vortex stretching.

The BET disk is the best compromise in terms of accuracy and cost, as it captures the flow phenomena happening in the unsteady case but at a fraction of the cost.

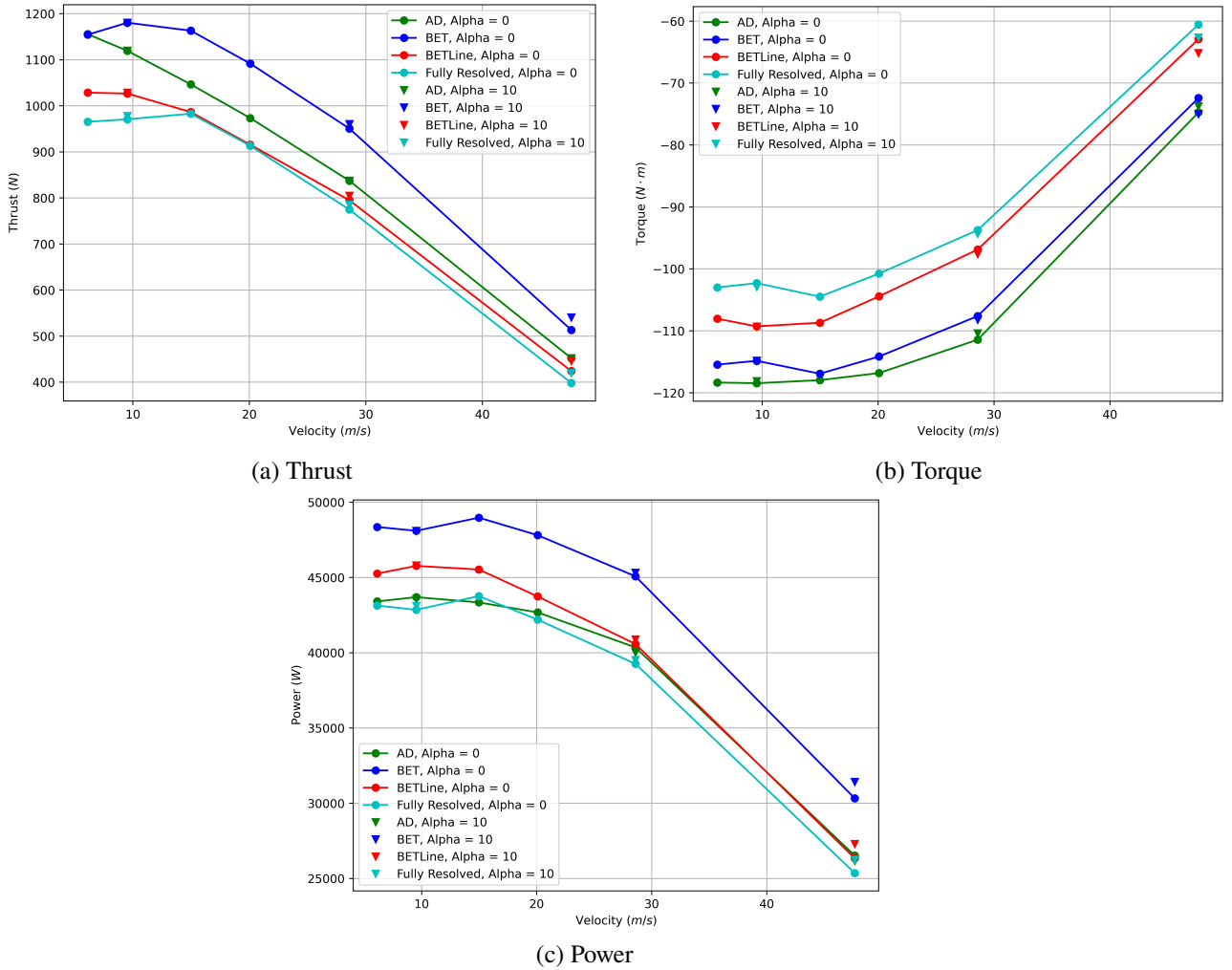
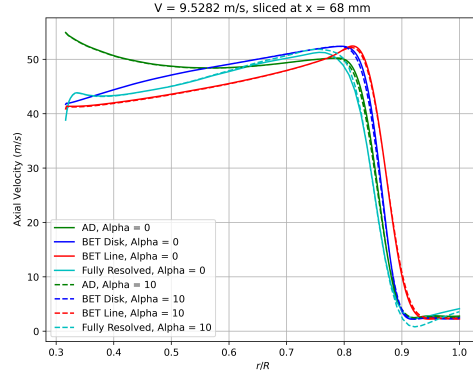
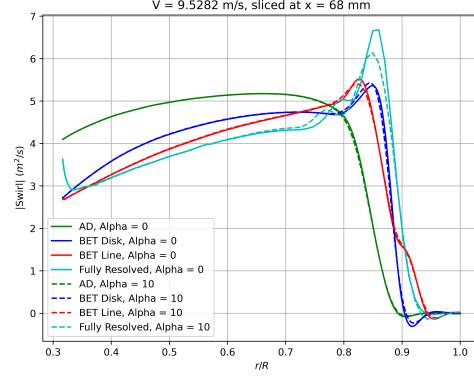


**Fig. 6 Thrust, torque, and power versus velocity for four propulsion models and angle of attack.**

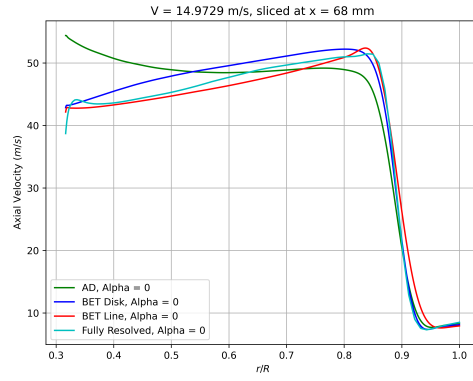




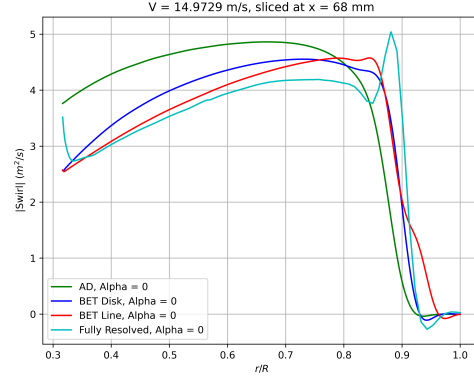
(a) Axial velocity,  $V_\infty = 9.53$  m/s



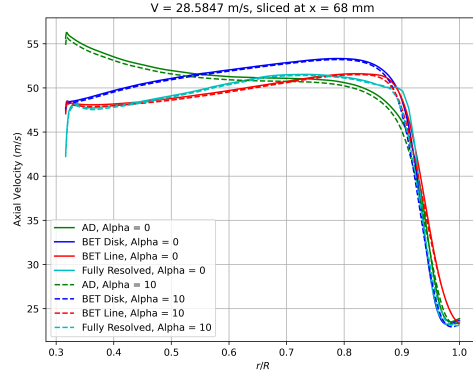
(b) Swirl,  $V_\infty = 9.53$  m/s



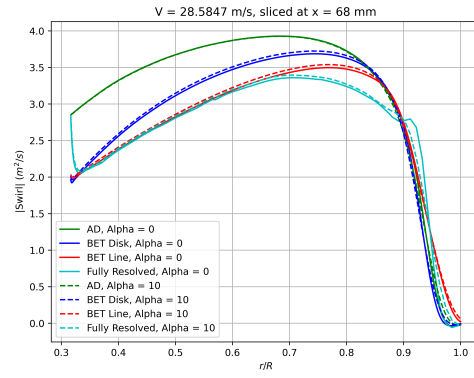
(c) Axial velocity,  $V_\infty = 14.97$  m/s



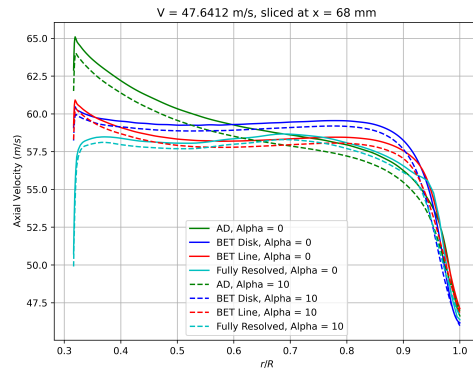
(d) Swirl,  $V_\infty = 14.97$  m/s



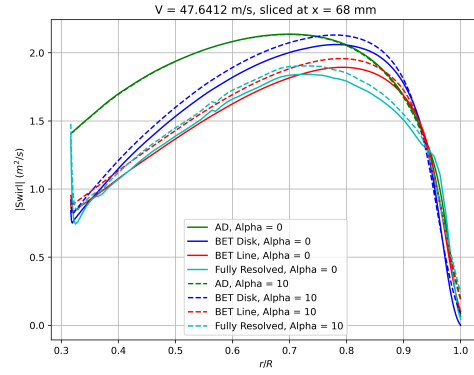
(e) Axial velocity,  $V_\infty = 28.58$  m/s



(f) Swirl,  $V_\infty = 28.58$  m/s



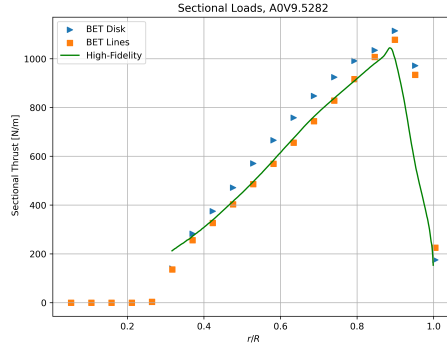
(g) Axial velocity,  $V_\infty = 47.64$  m/s



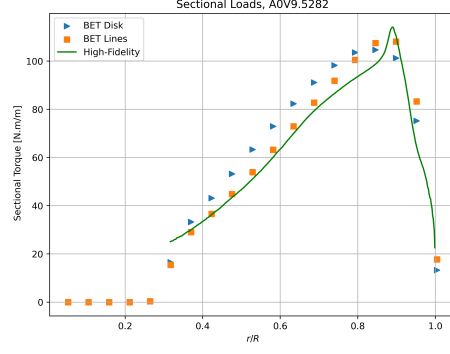
(h) Swirl,  $V_\infty = 47.64$  m/s

**Fig. 7 Comparison of the downstream wake for the four propulsion models for the speed sweep at  $\alpha = 0$  deg (solid lines) and  $\alpha = 10$  deg (dashed lines).**

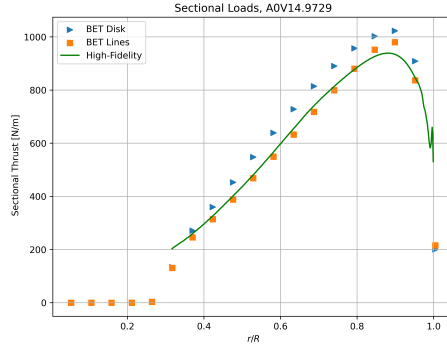




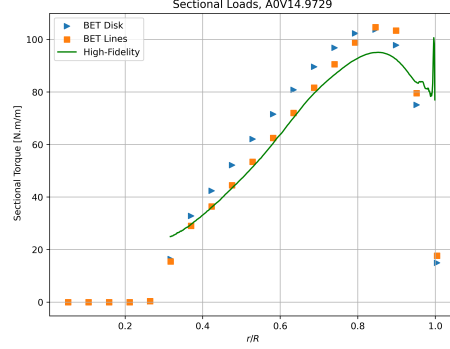
(a) Thrust,  $V_\infty = 9.53$  m/s



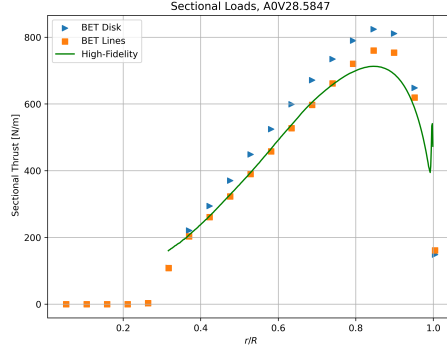
(b) Torque,  $V_\infty = 9.53$  m/s



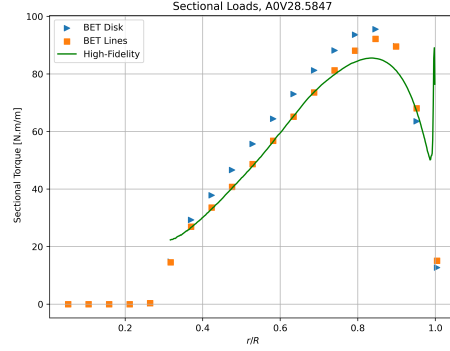
(c) Thrust,  $V_\infty = 14.97$  m/s



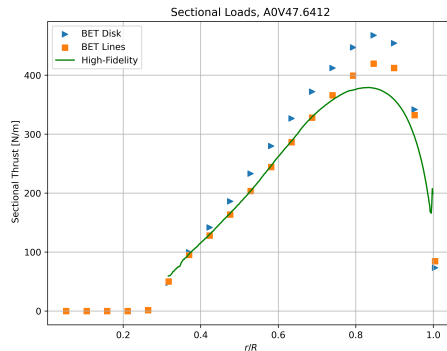
(d) Torque,  $V_\infty = 14.97$  m/s



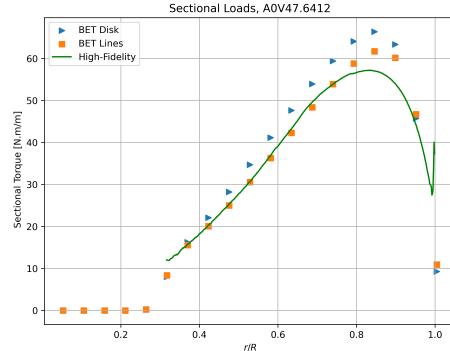
(e) Thrust,  $V_\infty = 28.58$  m/s



(f) Torque,  $V_\infty = 28.58$  m/s



(g) Thrust,  $V_\infty = 47.64$  m/s



(h) Torque,  $V_\infty = 47.64$  m/s

**Fig. 8** Sectional thrust and torque distribution for the BET and unsteady models at  $\alpha = 0$  deg.

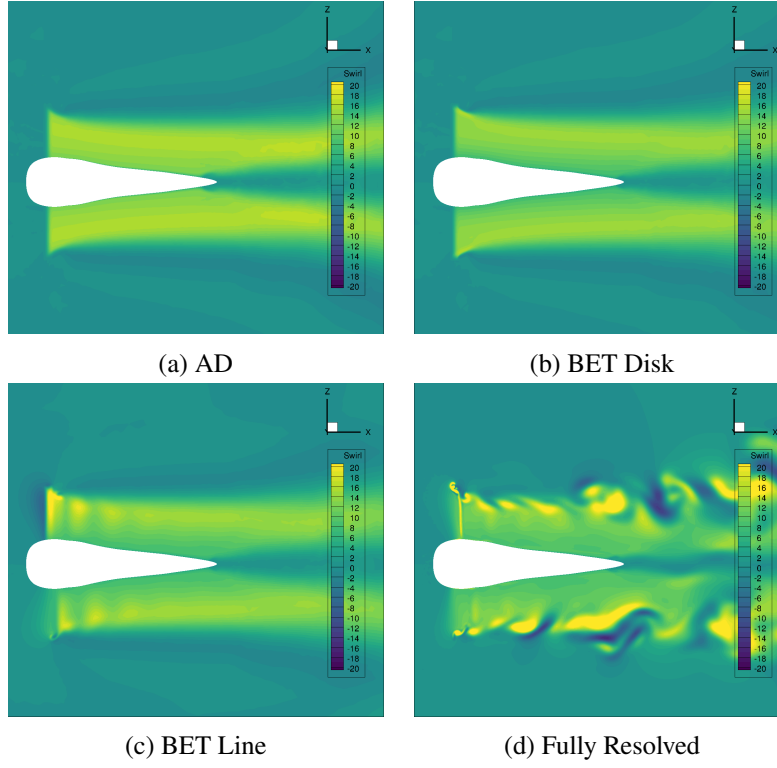


**Fig. 9** Contour of swirl for the four propulsion models at  $\alpha = 0$  deg and  $V_\infty = 9.53$  m/s.

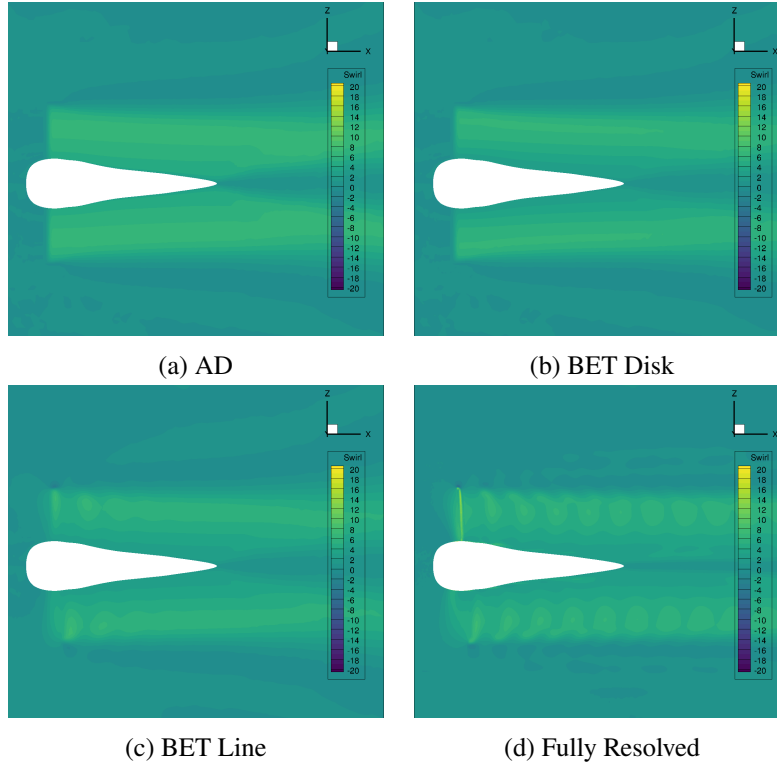


**Fig. 10** Contour of swirl for the four propulsion models at  $\alpha = 0$  deg and  $V_\infty = 47.64$  m/s.

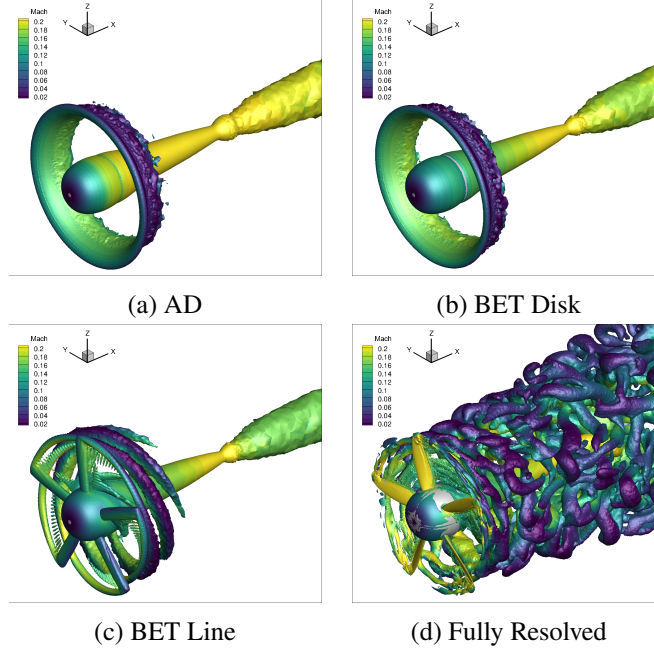


**Fig. 11** Q-criterion at  $\alpha = 0$  deg and  $V_\infty = 9.53$  m/s.

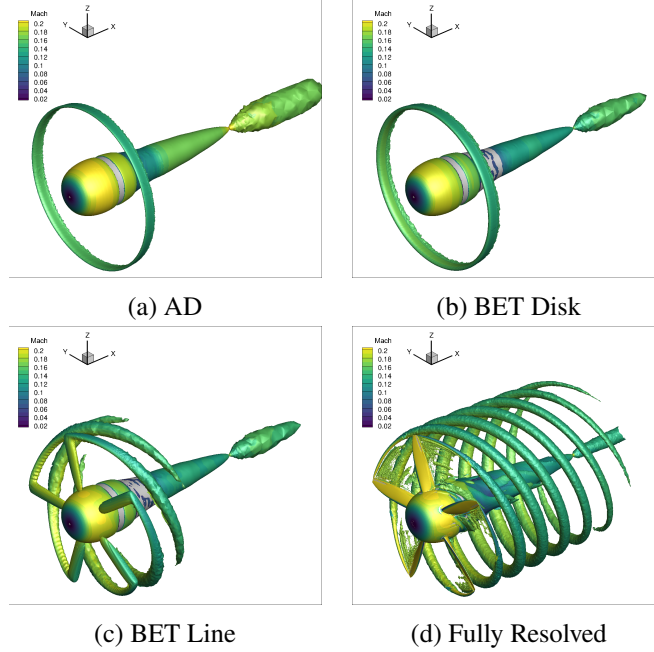


**Fig. 12** Q-criterion at  $\alpha = 0$  deg and  $V_\infty = 47.64$  m/s.

### B. Single-Rotor Model Problem

The isolated propellers results show that the BET disk model is a good compromise between accuracy and cost. First, this propulsion model was used to look at the effect of the different components, centerbody and pylon, which wakes interact with the flap system. Then, the effect of the propulsion model was looked at when varying angle of attack and power.

Conditions are shown in Tab. 5. Note that the corresponding propeller advance ratio falls in between the isolated propeller cases that were run.

**Table 5 Model Problem Flow Conditions.**

	BET disk	AD, BET disk, and BET line
$\alpha$ (deg)	[-10, -5, 0, 5, 10, 15]	[-10, -5, 0]
$T_c$	[2]	[1, 2, 3]
$V_\infty$ (m/s)	15.433	15.433
$\lambda$	0.114	[0.149, 0.114, 0.096]

### 1. Effect of Centerbody and Pylon

The aircraft as built will have centerbody and pylon for each propeller, and because their wakes interact with the high lift system, the designer needs to know their impact on the results.

Comparison of propeller  $C_T$  and  $C_Q$  for the different configurations and angle of attack is shown in Fig. 13, the full configuration (including both the centerbody and the pylon) and the no pylon configuration have minimal changes while the no pylon/centerbody has a 2% - 5% offset in  $C_T$  and  $C_Q$ .  $C_Q$  decreases with  $\alpha$  while  $C_T$  increases with  $\alpha$ .

The loads are added Fig. 14. Total includes contribution of the airframe only. The reference point for  $C_M$  is the propeller center.

The loads indicate that the main-element  $C_L$  increases until  $\alpha = 10$  deg, but the lift slope starts to reduce at different angle of attack depending on the configuration, and then decreases. In Figure 16, it can be seen that the main element boundary layer starts to thicken at lower angle of attack for the no pylon and no pylon/centerbody cases than the full geometry which could explain the  $C_L$  shape.  $C_D$  keeps increasing but notice the negative value until  $\alpha = 10$  deg. Another counter-intuitive feature in our results is that the apparent drag of the main element can be negative; this is not against any theorem, as long as the drag of the entire airfoil system is positive. The lift, drag and circulation of the elements separately means little. Besides, in such a strongly-coupled system, reporting drag and thrust separately is not rigorous. It is an asset of the model problem that such questions are posed in simple terms, which would be much less clear with 3D effects.

The flap  $C_L$  decreases with  $\alpha$ ,  $C_D$  first increases until  $\alpha = 5$  deg and then decreases when the flap reattaches. The vane behavior varies whether the full configuration, no pylon or no pylon and centerbody is considered. For the full configuration, vane  $C_L$  is mostly decreasing with  $\alpha$  and  $C_D$  increases. For the other two configurations, an increase in  $C_L$  happens, because of vane separation bubble that appears and then reattaches.

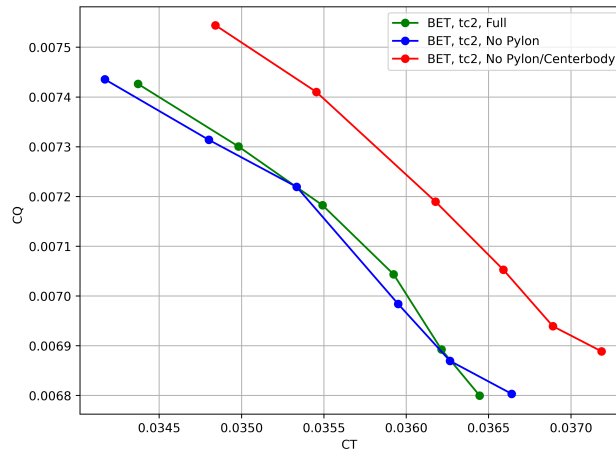


**Fig. 13  $C_Q$  vs  $C_T$  for different configurations.**

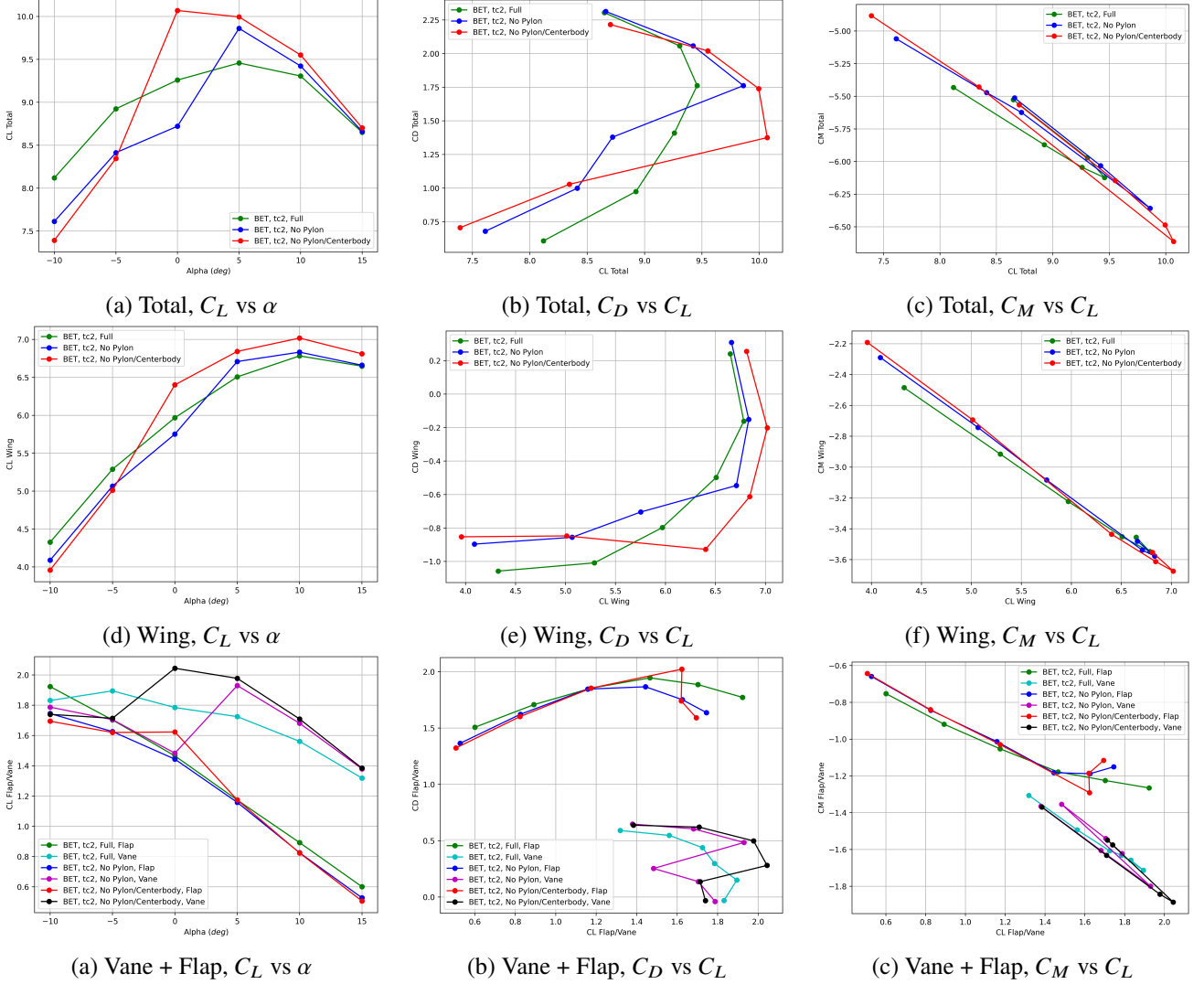


**Fig. 14 Integrated Loads comparisons between different configurations**

Visualization plots comparing the geometry with pylon and centerbody, with centerbody only, and without either of them are shown in Fig. 15, 16, 17, and 18. The skin friction coefficient plots, shown in the bottom view, indicate that the flow behavior is similar for the three cases. As angle of attack is increased and more lift is generated from the main element, the skin friction coefficient naturally increases at the wing leading edge. When looking at the top view, a drop in skin friction coefficient appears around the middle line as angle of attack increases showing that the main element starts to separate, presumably because more fluid with a loss of total pressure bathes this region. This drop is stronger with the no pylon/centerbody case. The full configuration has a separation bubble in the middle of the flap from  $\alpha = 5$  deg until  $\alpha = 5$  deg while the geometries with centerbody only or no pylon/centerbody only indicate a drop in skin friction coefficient. For the no pylon and no pylon/centerbody configurations, the flap only separates at  $\alpha = -10$  deg. The flow on the vane is also dependent on the configuration.

Separation at low or even negative angles of attack and not at higher angle of attack is counter-intuitive, but it is also encountered over unblown configurations with high flap deflection, for instance at high-lift prediction workshops. The mechanism is the following: at higher angles of attack, the lift on the main-element increases, the circulation around increases, and this enhances the downwash near the flap, thus allowing it to reattach. Another interpretation is that at low angle of attack, all the lift is created by camber and "stresses" the flap. With increasing angle of attack, the added lift has a preponderance on the front of the airfoil. Within thin-airfoil theory, the *incremental* pressure difference between

upper and lower surface associated with angle of attack has its centroid at the 1/4-chord point.

It is also noted from the swirl plots that having the full configuration reduces the swirl downstream. This is also true as angle of attack increases as most of the jet flow is directed upward towards the centerbody, pylon, and wing.

In addition to the swirl and skin friction plots shown previously, plots of total pressure coefficient are shown. Definition is given in App. VIII. At  $\alpha = -5$  deg, the centerbody starts to separate. The difference in flap separation can be seen from the loss region being dominant in the full configuration for  $\alpha = -5$  deg at the propeller centerline. The region where more energy is added to the flow is bigger on the wing suction side at higher angle of attack causing the flap to be less effective at turning the jet flow. At  $\alpha = 5$  deg, it is clear that the main element boundary layer is thicker for the no pylon and no pylon/centerbody cases.

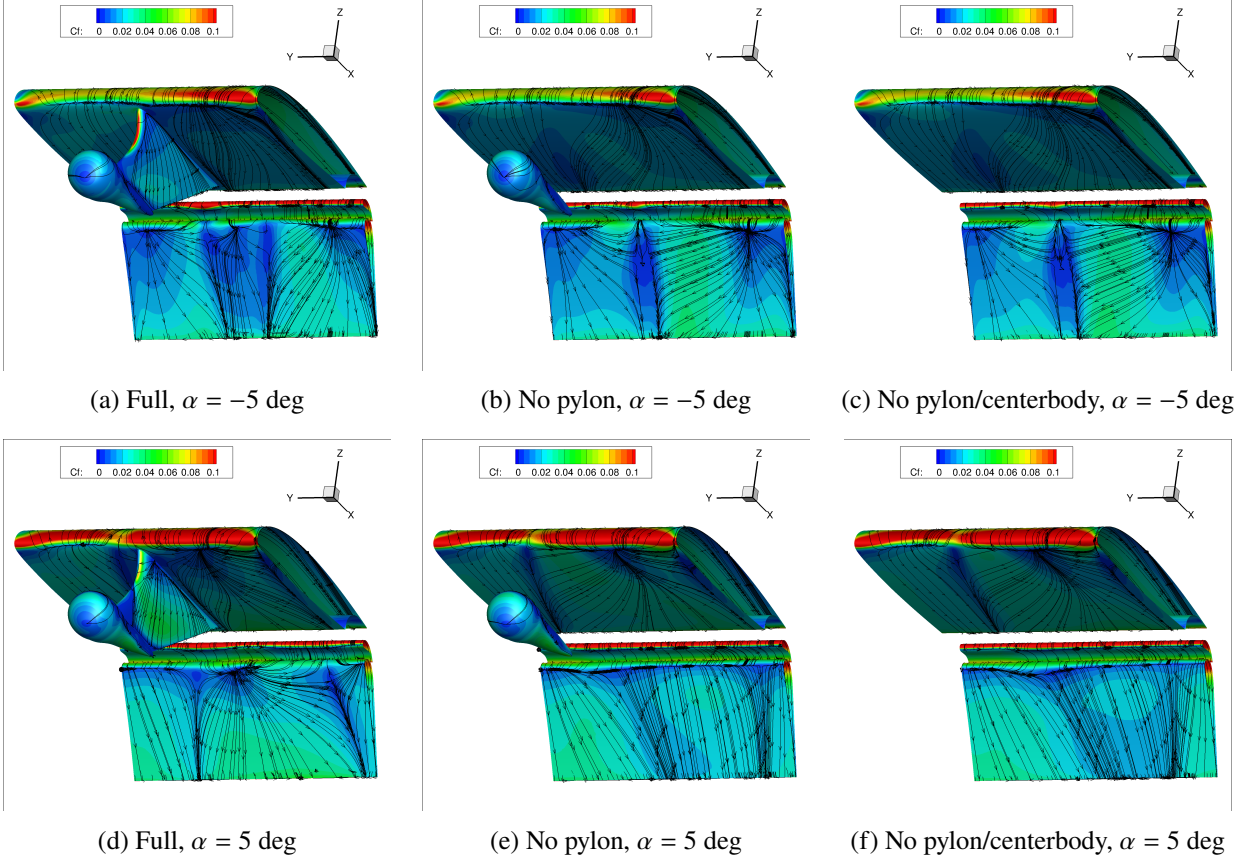


**Fig. 15 Skin friction coefficient, bottom view, for the different configurations and  $\alpha = \pm 5$  deg.**



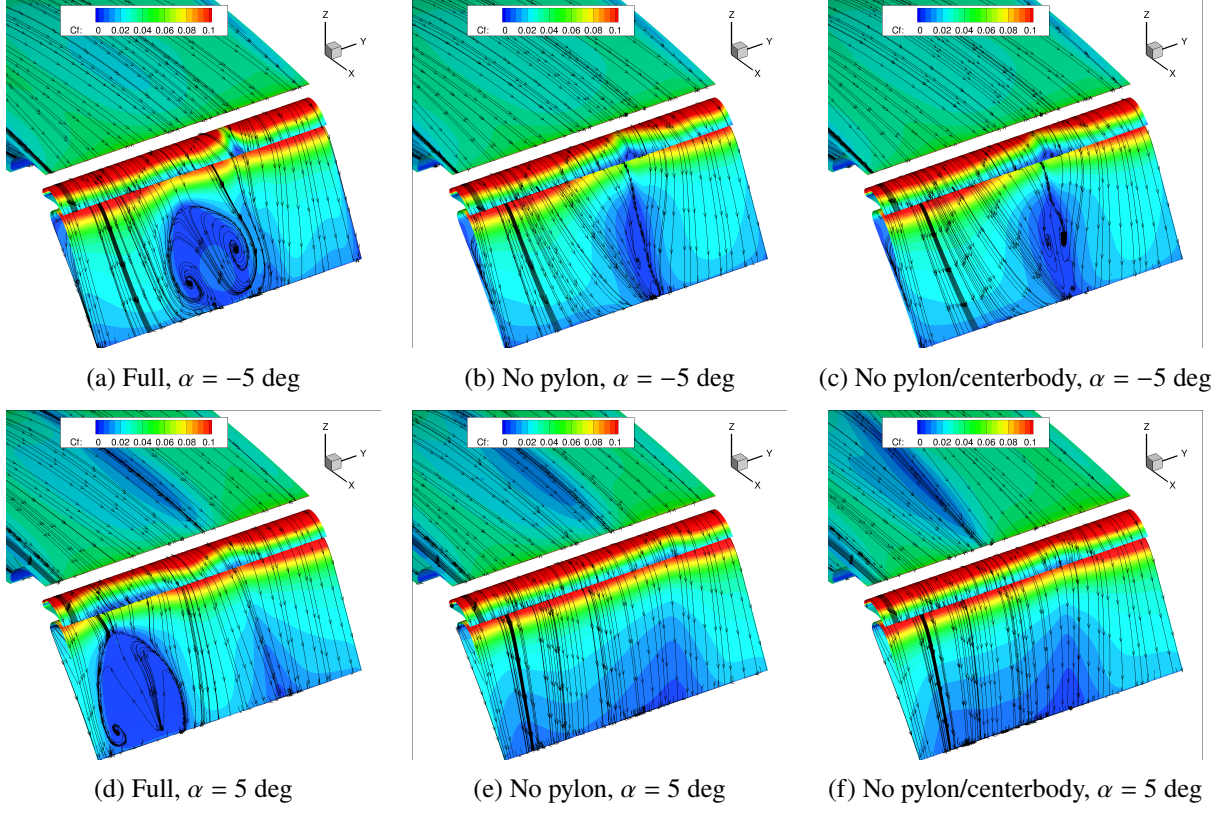


**Fig. 16 Skin friction coefficient, flap view, for the different configurations and  $\alpha = \pm 5$  deg.**

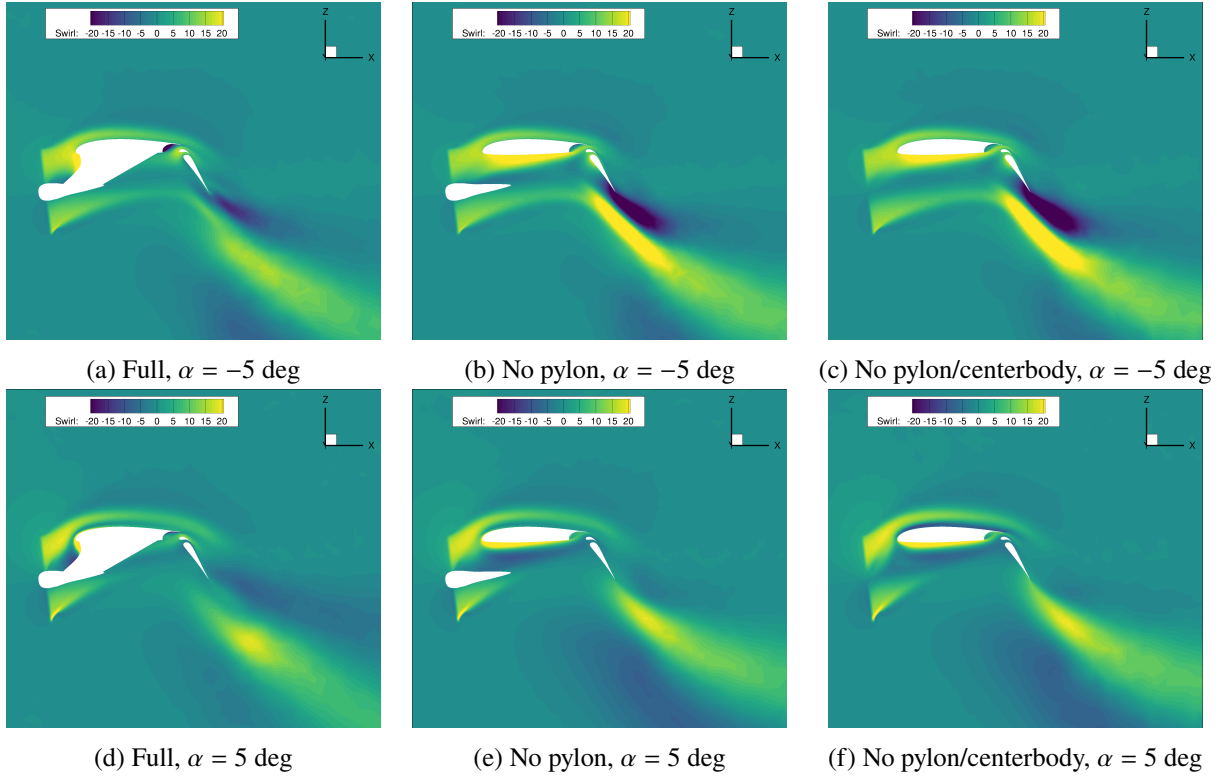


**Fig. 17 Contour of swirl at propeller centerline for the different configurations and  $\alpha = \pm 5$  deg.**

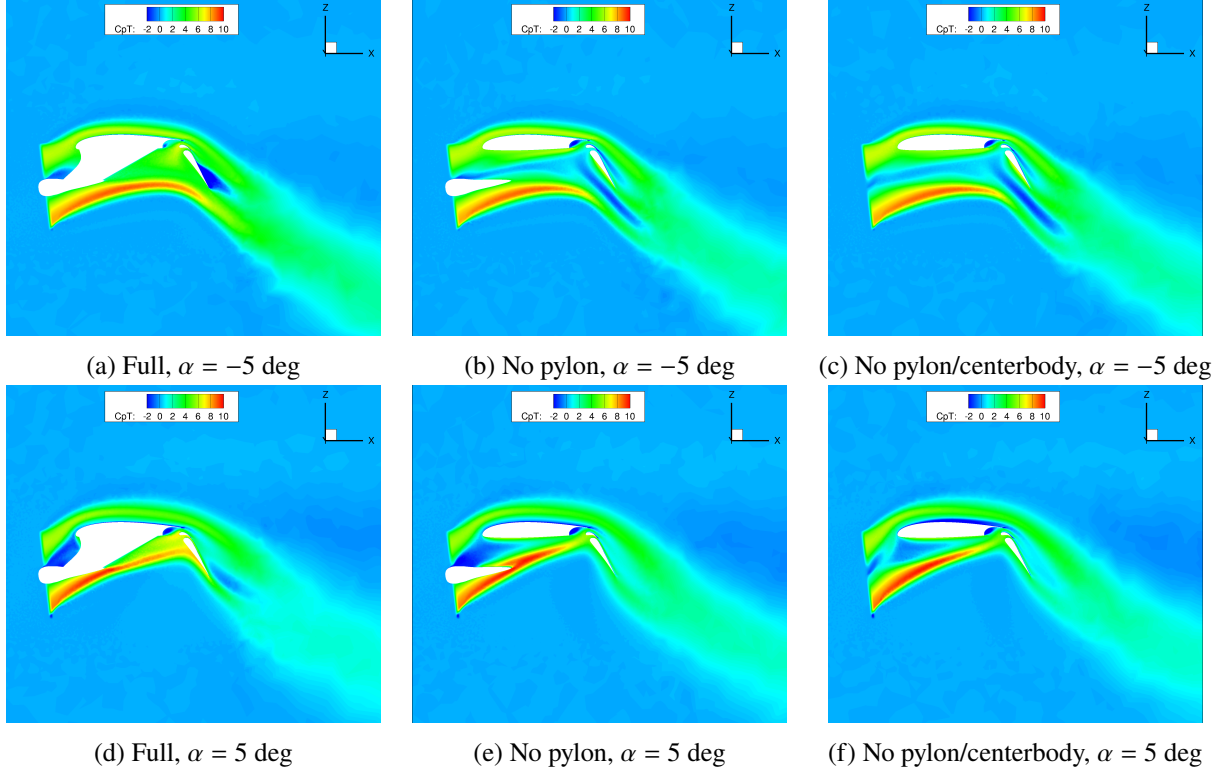


**Fig. 18 Contour of  $C_{p_i}$  at propeller centerline for the different configurations and  $\alpha = \pm 5$  deg.**

In summary, the presence of the pylon is important as it reduces the swirl magnitude and it impacts when the separation on each element happens. For the following sections, the full configuration was chosen as the reduction in mesh points was not enough to win.

## 2. Effect of Propulsion Model

The propulsion model was varied along with  $\alpha = [-10, -5, 0]$  deg and  $T_c = [1, 2, 3]$ . The BET line and the full unsteady simulations were run for only one condition,  $\alpha = -5$  deg and  $T_c = 2$ . Note that satisfactory convergence was not achieved for the full unsteady case, the solution is oscillating and still changing for some components, thus those results have a lot of uncertainties. We are still showing the results nonetheless.

The coefficients  $C_T$  and  $C_Q$  for AD, BET disk and line and the unsteady runs for the full sweep of angle of attack are added to Fig. 19.  $C_Q$  numbers for AD are higher than BET and the difference increases with  $T_c$  (6% at  $T_c = 3$ ) but  $C_T$  is smaller and the difference decreases with power (15% at  $T_c = 1$ ). It was not expected for thrust differences to be larger than torque differences; thrust differences appear to be strongly affected by the flow distortion. Note that the AD thrust does not change with angle of attack since that is an input from the user. When comparing to the BET line, the  $C_Q$  at  $\alpha = -5$  deg,  $T_c = 2$  is similar but  $C_T$  is higher by 10% in the BET disk. The unsteady  $C_T$  and  $C_Q$  are 20% lower than the BET disk, so less power is added to the flow, this is attributed to the poor convergence and further work is needed to fully resolve this issue.

The wing loads are shown in Fig. 20. When looking at the  $C_L$  plot, a few things can be concluded, in particular the lift slope increases with  $T_c$  which means higher  $C_{L_{\max}}$  can be achieved at higher  $\alpha$  with  $T_c$  (flap is more effective at turning the jet flow). At low  $T_c$ , AD and BET disk are not too far apart even though AD predicts a decrease in  $C_L$  from the main-element and the flap before BET does. As  $T_c$  increases, the difference between AD and BET grows and grows even more with decreasing angle of attack (impact of swirl). When comparing to the BET line flow condition, the flap  $C_L$  and  $C_D$  are well captured both by AD and BET disk, while the vane  $C_L$  is 10% higher for BET disk (26% for AD) but the  $C_D$  is similar for both AD and BET disk. The main-element  $C_L$  is higher for BET disk by 20% (25% for AD), and its  $C_D$  is higher by 33% (47% for AD). These are very large differences. The lift-curve slope is of interest; in some regions it is small, near maximum lift, and in other regions it is larger than  $2\pi$ . The unsteady flap  $C_L$  and  $C_D$  are



very close to the BET line, the vane  $C_L$  is 10% lower in the unsteady case in comparison to BET line. The unsteady main-element  $C_L$  drops by another 10% from the BET line, it is mainly attributed to the decrease in power.

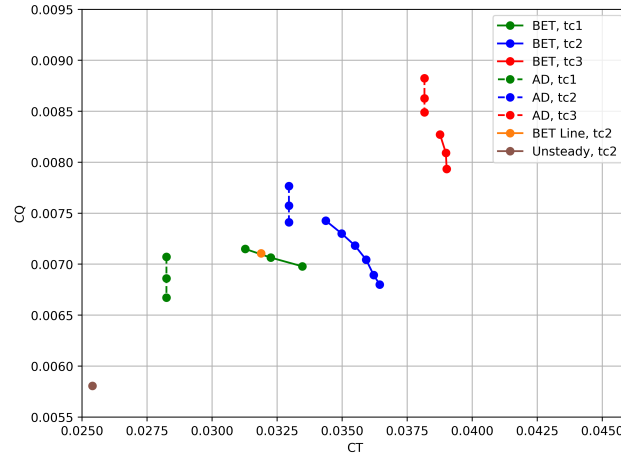


**Fig. 19**  $C_Q$  vs  $C_T$  for different models and power levels. Each line is an angle-of-attack sweep.

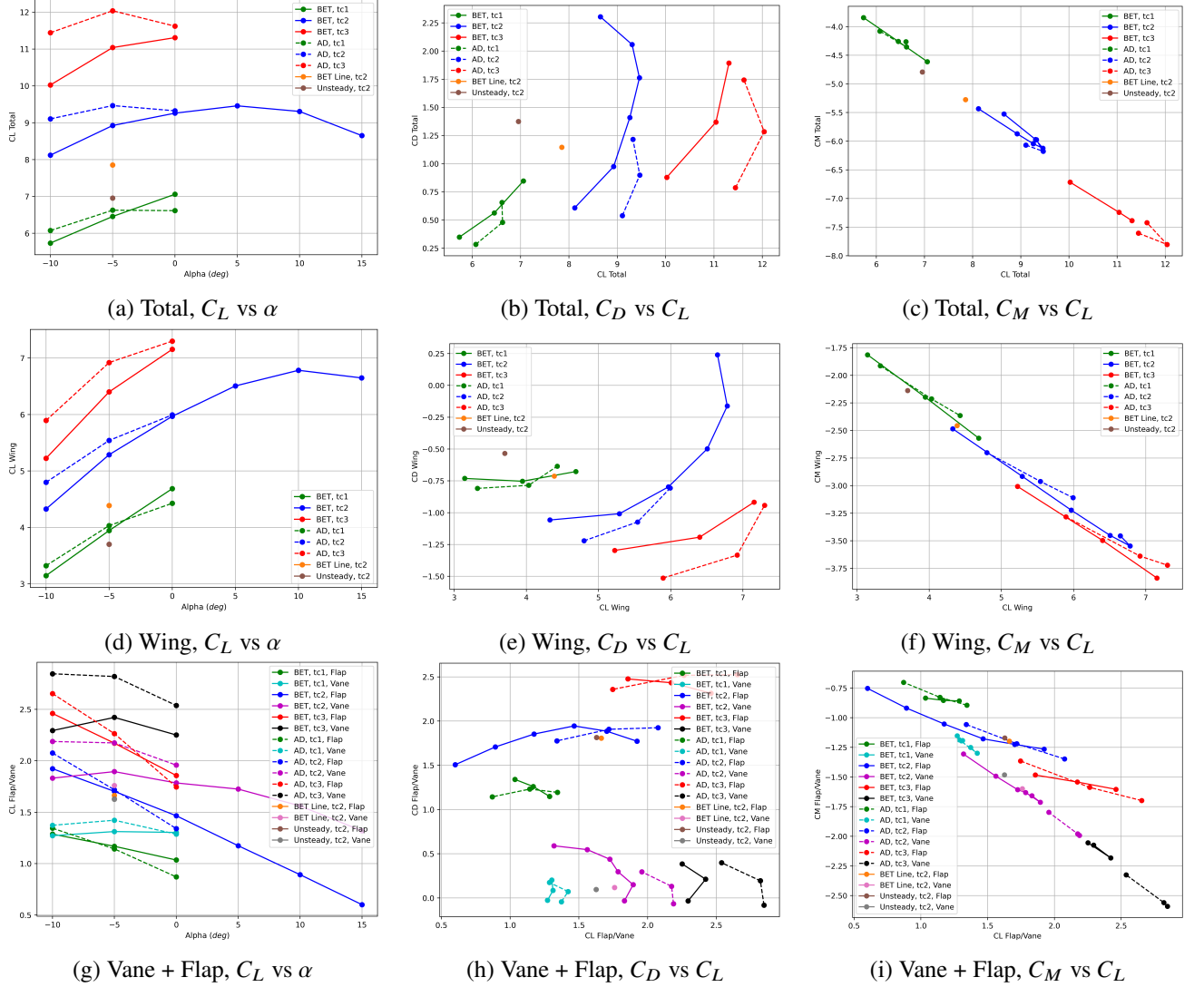


**Fig. 20 Integrated wing Loads comparisons between rotor models and power levels**

As mentioned previously, Fig. 21 shows that  $T_C$  suppresses the flap separation and increases skin friction coefficient in general.

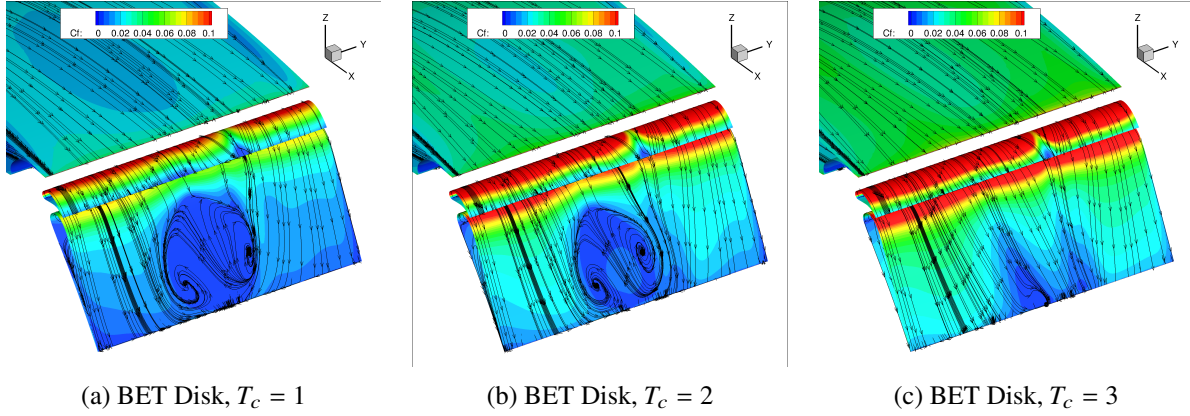


**Fig. 21 Skin friction coefficient, flap view, effect of  $T_c$  for BET disk at  $\alpha = -5$  deg**

Skin friction coefficient plots, Fig. 22 and 23, show that the actuator disk predicts a higher level on the centerbody and the wing leading edge. BET disk overpredicts the skin friction coefficient on the wing leading edge in comparison to BET line, which itself is slightly higher than unsteady. Both AD and BET disk have flap separation while BET line and unsteady only show a drop in skin friction coefficient. This could be tentatively explained by the fact that the BET line and the full-blade models introduce effective turbulence in the rotor's streamtube. A weakness of this conjecture is that the turbulence does not contain length scales small enough to couple with the boundary-layer turbulence; a flow region is not "either turbulent or non-turbulent".

It must be remembered that, in regions with generally weak skin friction, small absolute changes in the skin-friction vector can cause large variations in the surface flow pattern, including crossing over from "attached" to "separated." Reversed flow at the wall also does not always reflect any kind of "massive" separation. However, here, Fig. 25 (b) does show a significant departure from the flap surface.

The  $C_{p_i}$  plots, Fig. 25, also show that the AD predicts high energy flow around the vane when it is reduced for the BET and unsteady models. The BET line and unsteady figures contain dark blue spots which would be anomalous in a steady flow, carried by the vortices. Again, total pressure is a quantity created to interpret steady flows which satisfy Bernoulli's steady equation; this introduces distracting features in unsteady flow fields. The  $C_{p_i}$  plots show that with BET line and unsteady more energy is added to the flow in front of the rotor by the propeller on the bottom side, but that is not seen with the two steady models. The reason is that one of the blades is pointing down, and its front side carries a lower static pressure and a perturbation of the velocity magnitude; this feature would pulsate at the blade-passing frequency in an animation.

Contours of swirl are added Fig. 24, differences can be seen around the vane and flap, AD and BET disk have smaller magnitude of swirl at the flap. As expected, the propeller swirl is closer to BET line and unsteady for the BET disk than the AD.

Q-criterion plots Fig. 26, and 27 show the same propeller behavior as isolated propeller results where the propeller shear layer for AD and BET disk is impacting the wing/flap system differently than the tip vortices from the BET line and unsteady case. The unsteady case shows a new vortex going sideways from the blade tip, that we think is due to poor convergence in time, in other words residual effects of the simulation start. This will be explored in revisions of this paper.

The interpretation of the Q-criterion is complicated by several facts. First, the surfaces depend on the level chosen, and the Q-criterion can appear to "vanish" although it has simply decayed somewhat. Second, the criterion marks curved vortex layers even though they would not be clearly viewed as "vortices." A similar phenomenon is how the Q-criterion marks the boundary layers on convex surfaces, because the curvature makes the vorticity exceed the strain, but these regions are most definitely not vortices. Finally, numerical and turbulent diffusion ultimately makes successive tip vortices merge, creating a corrugated shear layer followed by a smooth one, in which the criterion drops; a finer grid or a different turbulence model could have prevented or delayed this.

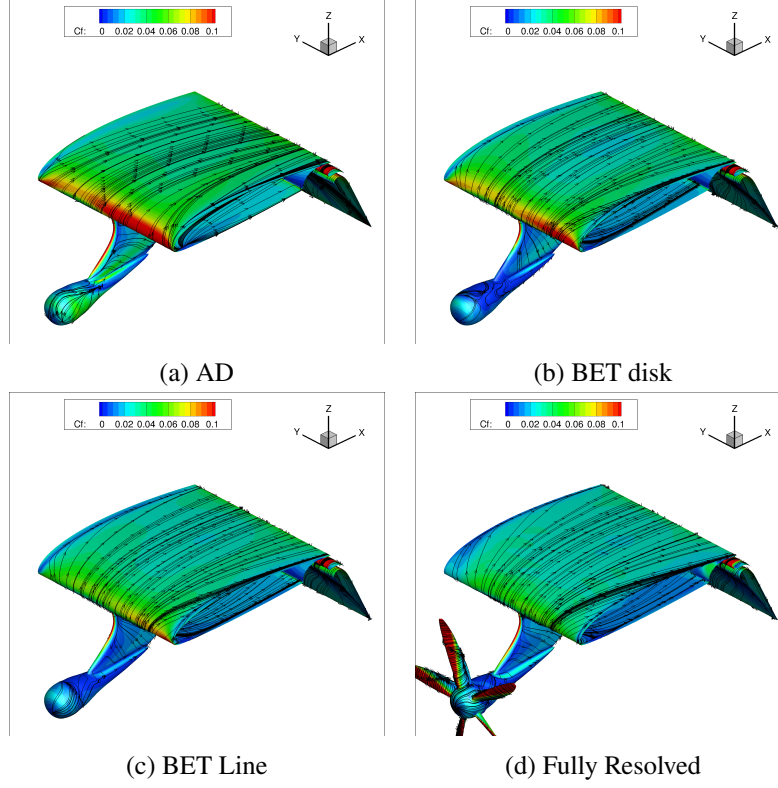


**Fig. 22** Skin friction coefficient, top view, for the different propulsion models at  $\alpha = -5$  deg.

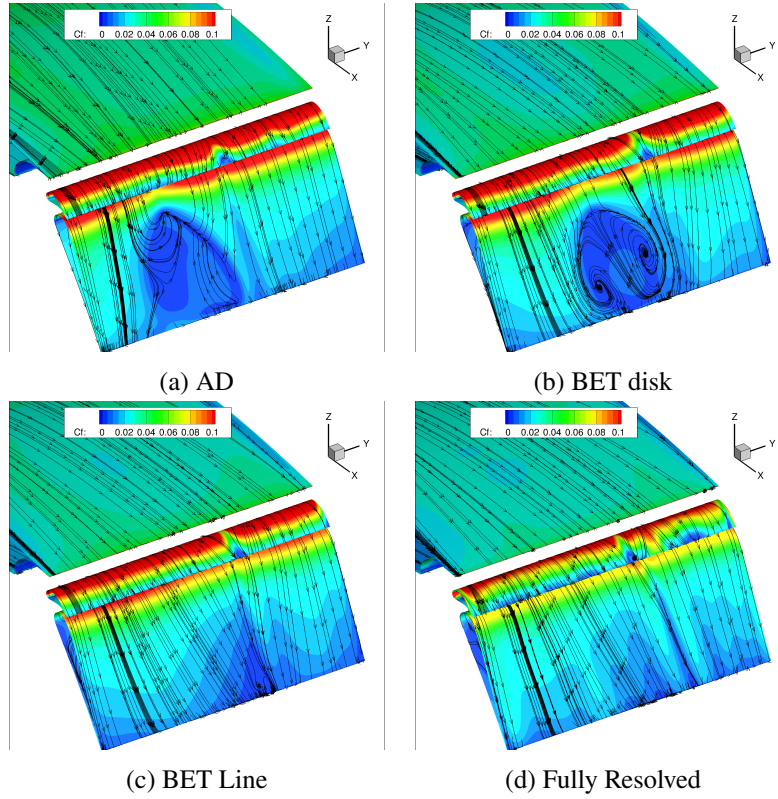


**Fig. 23** Skin friction coefficient, flap view, for the different propulsion models at  $\alpha = -5$  deg.

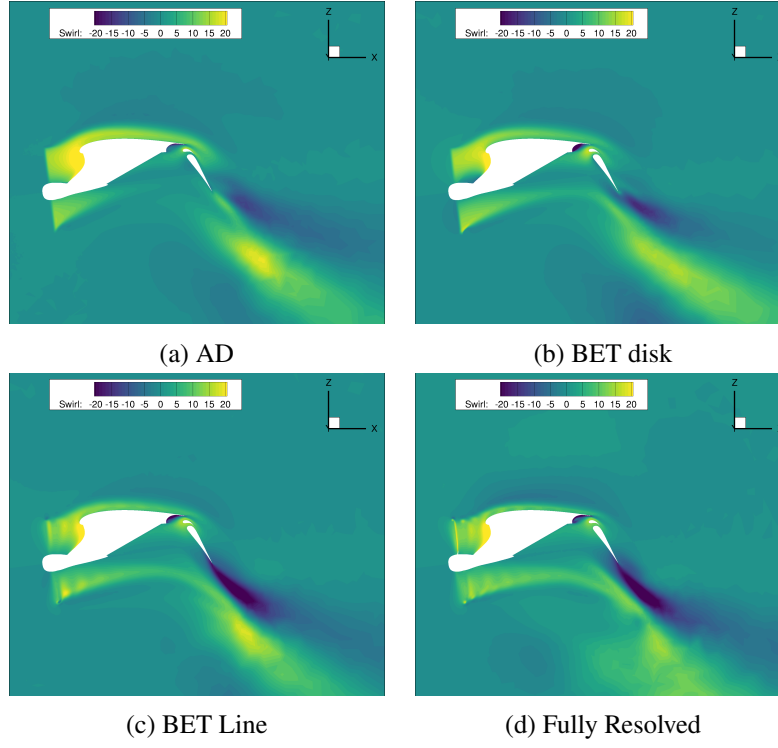


**Fig. 24** Contour of swirl at propeller centerline for the different propulsion models at  $\alpha = -5$  deg.

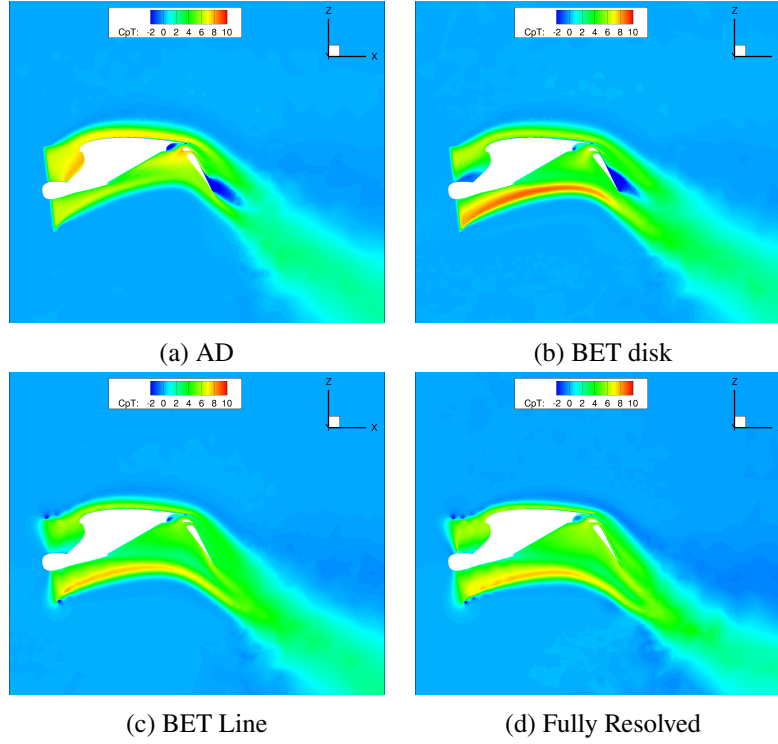


**Fig. 25** Contour of  $C_{p_t}$  at propeller centerline for the different propulsion models at  $\alpha = -5$  deg.

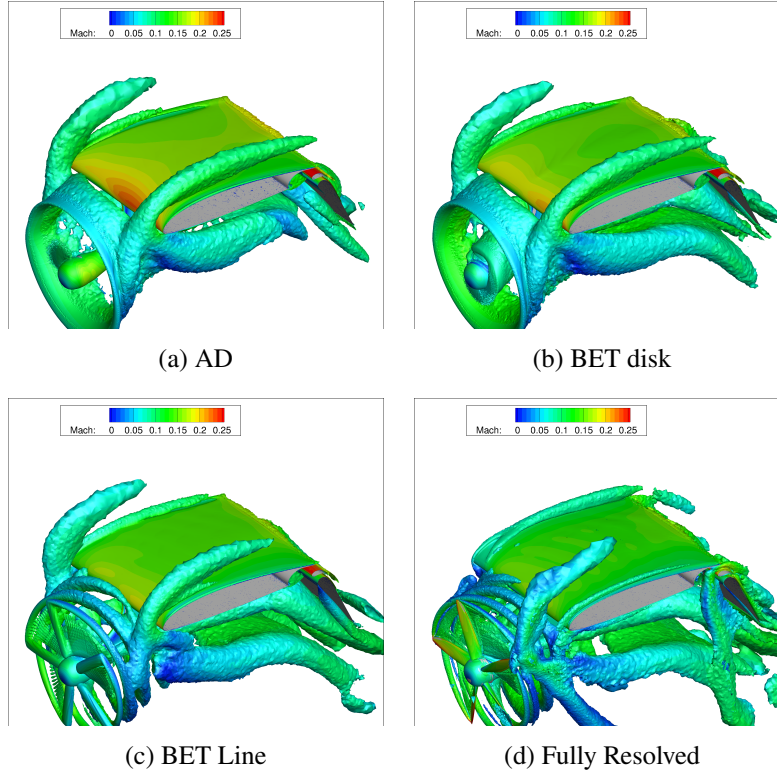


**Fig. 26** Q-criterion plots, front view, for the different propulsion models at  $\alpha = -5$  deg.

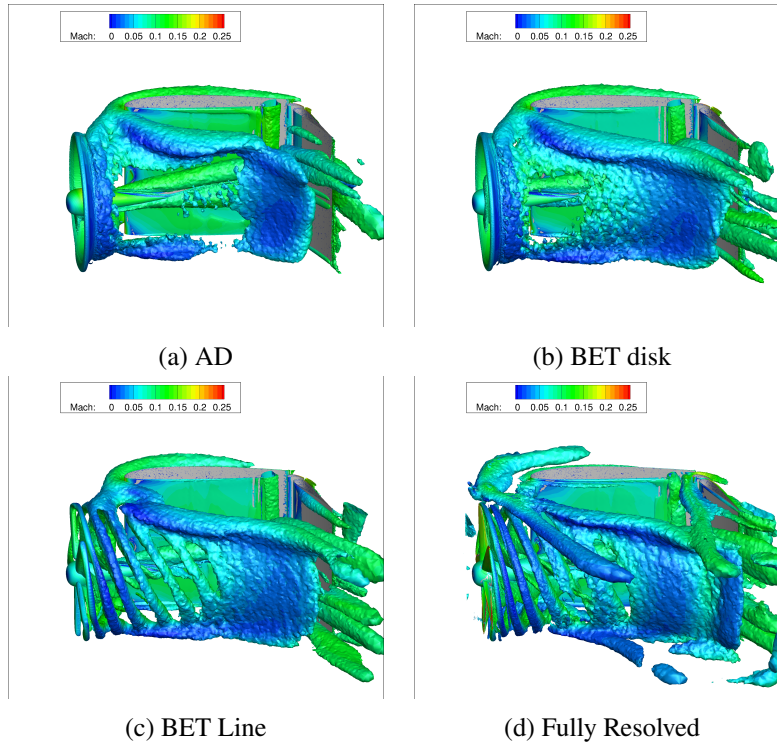


**Fig. 27** Q-criterion plots, side view, for the different propulsion models at  $\alpha = -5$  deg.

This section shows that it is important to model all the geometries that interact with the propeller wake as it impacts both the local flow and the integrated  $C_L$ ,  $C_D$ , and  $C_M$ .

The BET disk results are closer to the BET line than AD and visualization plots show that BET disk captures more of the flow physics. Due to resource limitation for this paper, we only had one condition for the BET line and unsteady but an alpha sweep could be performed to compare  $C_{L_{max}}$  and further evaluate the difference between AD, BET disk, and BET line.

Because of the poor convergence of the unsteady case and the fact that it has lower power inputted to the flow, it is not surprising that its  $C_L$  is lower too.

### C. 3D Geometry Results

A few cases were run for the 3D geometry for comparison with the model problem where power and angle of attack were varied, the conditions are summarized in Tab. 6.  $T_c$  values match between the model problem and the 3D geometry as the 3D geometry has four propellers and four times more area. Note that the 3D geometry is not entirely representative of the model problem as there is a flap break between propellers 2 and 3 which breaks the symmetry assumption but the propeller spacing is the same. The results from angle of attack and power effects for different propulsion models are not shown as the same conclusions can be drawn from the model problem.

**Table 6 3D Flow Conditions.**

	AD, and, BET disk	BET line
$\alpha$ (deg)	[10, 15]	15
$T_c$	[2, 3]	2
$V_\infty$ (m/s)	15.433	15.433

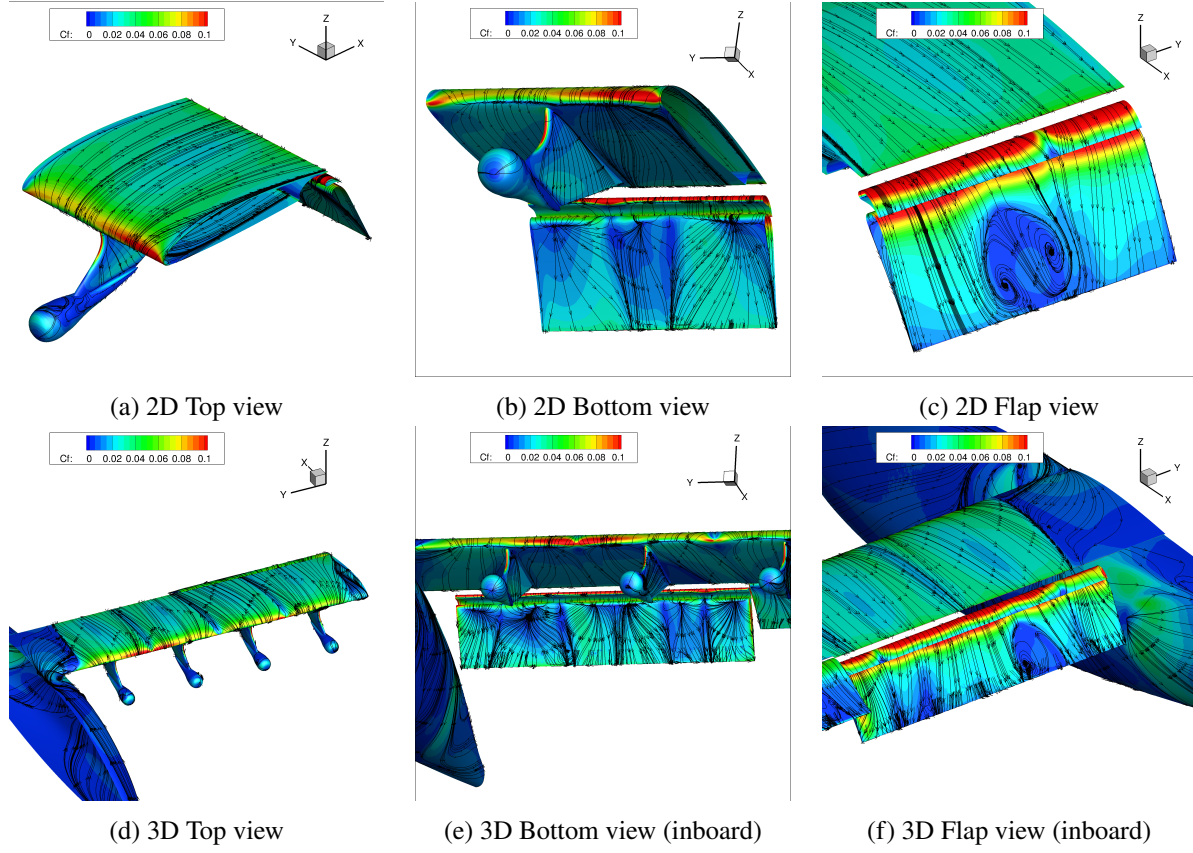
We focus the comparison using the BET disk between the model problem and the 3D geometry that is model problem at  $\alpha = -5$  deg,  $T_c = 2$ , and 3D geometry at  $\alpha = 15$  deg,  $T_c = 2$  indicating an induced angle of 20 deg.

The skin friction coefficients Fig. 28 show similar characteristics for the inboard portion of the wing, especially for propeller 4 where there is a lower skin friction coefficient region on the suction side of the wing, on the vane, and on the flap. The swirl magnitude is reduced in the 3D case when comparing the isolated rotor with the 3D rotors 3, and 4 but that could be due to the presence of the fuselage, on rotor 3 a high positive region of swirl is shown at the bottom of the picture, potentially from the flap break vortex. The energy levels can be compared in Fig. 30, the same thickness of the propeller top high energy flow covers the wing, the bottom high energy flow is hitting the flap differently whether we are looking at propeller 3 or 4 but at propeller 4 centerline the flap separation is present as in the model problem.

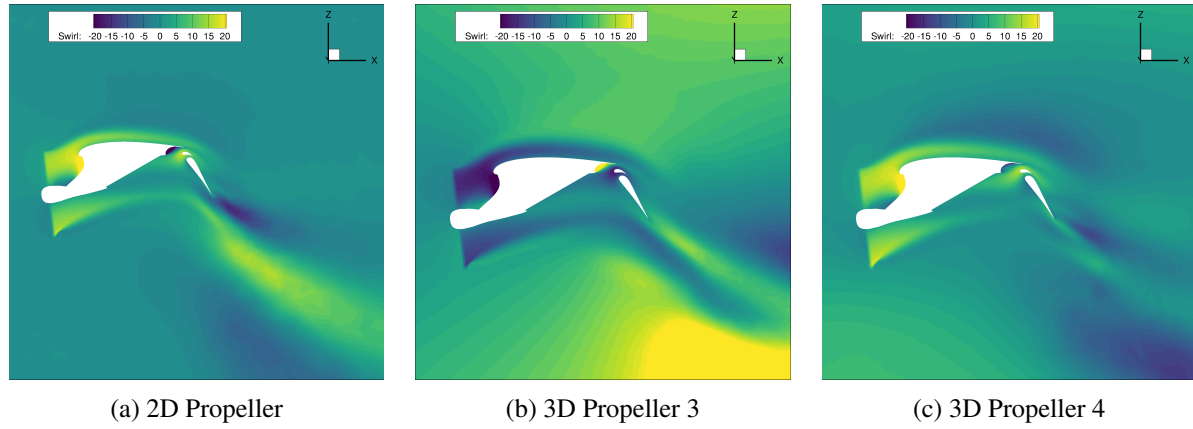
When looking at propeller  $C_T$  and  $C_Q$ , performance for the different propellers is indistinguishable in Fig. 31. The difference between the model problem, Fig. 19, and the 3D geometry is minimal. This is highlighted by looking at the intersection of the black plain lines, which corresponds to the 2D condition, and the black dashed lines (propeller 3) and grey dashed lines (propeller 4) which corresponds to the 3D condition.

Figure 32 shows the integrated loads for the 3D condition. The moment reference point is forward and below the airplane nose. The same conclusion as the model problem can be drawn for the effect of  $\alpha$ ,  $T_c$  and AD/BET disk. When looking at BET line, the performance is much closer ( $C_L$  4%) to BET disk than in the model problem. When comparing to 2D though, Fig. 20, it can be noticed that the achieved  $C_L$  are much lower in the 3D configuration, part of the difference can be attributed to the non-uniform loading on the wing due to fuselage contribution, flap break and aileron outboard wing.





**Fig. 28** Skin friction coefficient for different views. (a-c): 2D,  $\alpha = -5$  deg. (d-f): 3D,  $\alpha = 15$  deg.  $T_c = 2$  for both 2D and 3D cases.



**Fig. 29** Contour of Swirl. (a): 2D  $\alpha = -5$  deg. (b-c): 3D  $\alpha = 15$  deg.  $T_c = 2$  for both 2D and 3D cases.



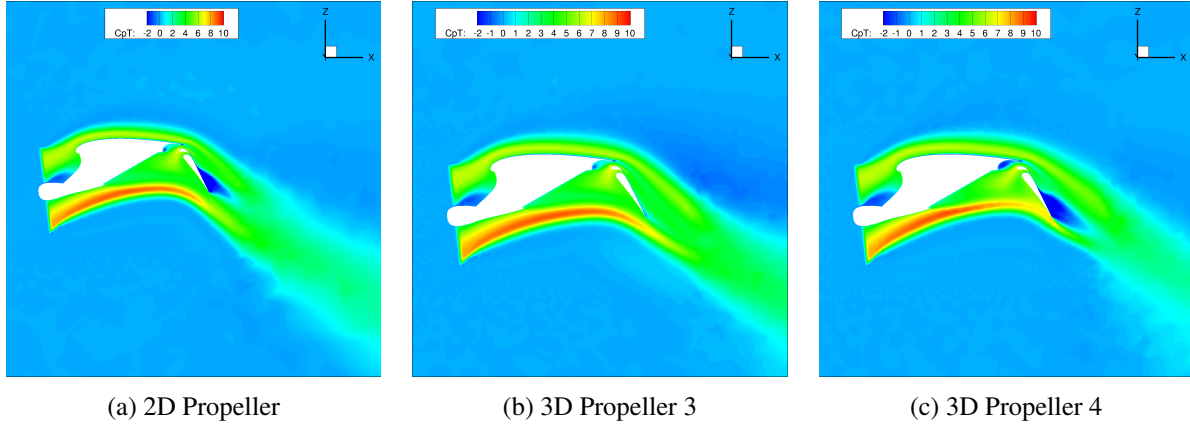


**Fig. 30** Contour of  $C_{p_i}$ . (a) 2D  $\alpha = -5$  deg. (b-c) 3D  $\alpha = 15$  deg.  $T_c = 2$  for both 2D and 3D cases.

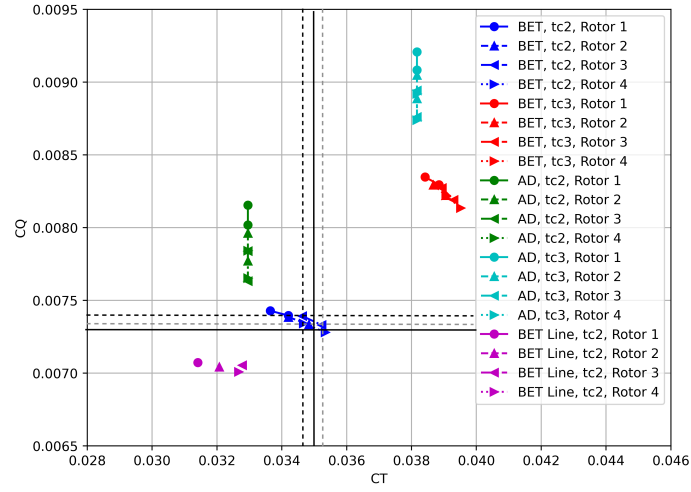


**Fig. 31**  $C_Q$  vs  $C_T$  for different configurations.

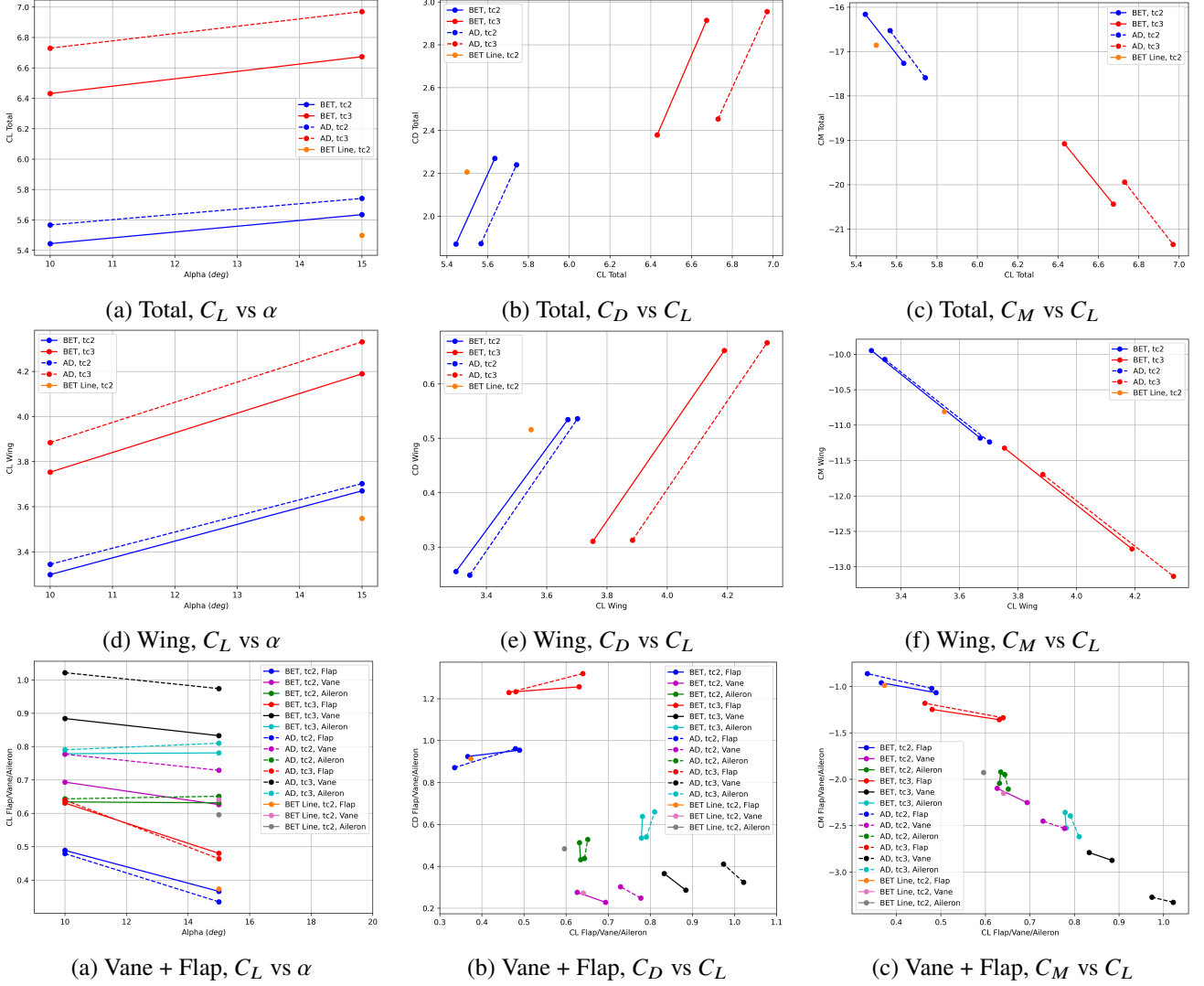


**Fig. 32 Integrated Loads comparisons between different configurations**

The computational cost differences between different models and the 2D model/3D problems is summarized in Table 7. The first thing to note is that here is no difference in cost between AD and BET disk. The values in the table are normalised to the isolated Propeller AD/BET disk simulation cost. Ranges are given when it depended on the flow condition. It can be seen that using AD/BET disk compared to BET line offers a speed up factor of 12-20 depending on the problem studied. For the isolated propeller, the AD and BET disk simulations used a grid of 6.9M cells whereas the resolved blades simulation used a grid of 18.1M cells which is also part of the lower simulation cost for the AD/BET models. The difference between the model problem and 3D problem is a factor of 8 for the steady AD/BET Disk simulations and a factor of 4 for unsteady BET line simulations. For the unsteady simulations, the speed up factor is similar to the factor difference in the mesh sizes. For steady simulations, the 2D model problem converges to the desired residual tolerances ( $1e-10$  for flow,  $1e-8$  for turbulence), whereas the residual start to stagnate for the 3D problem at  $1e-7$  (due to some unsteadiness), increasing the benefit of the 2D model problem simulation cost. For unsteady blade line simulations, the 2D model problem was simulated for 40 revolutions, whereas the full 3D geometry was simulated for 35 revolutions, using 3 degree time steps.

**Table 7 Computational cost for 2D model problem and 3D solution using different rotor models. Values normalised to the AD/BET isolated propeller simulation cost.**

	AD, and, BET disk	BET line	Resolved Blades
Isolated propeller	1.0	6-12	40-60
2D model problem	3-4	80	-
3D	25.0	320	-

## VI. Conclusion

This work continues our effort towards the accurate modelling of blown wings by demonstrating the performance difference of four propulsion models, namely, an actuator disk, a blade-element model run in a steady and an unsteady formulation, and a time-resolved simulation of the full propeller geometry. The geometries incrementally increased in complexity to capture the effect of various components, from an isolated propeller to a single-rotor combined with a wing and high lift device (model problem) to the full 3D geometry. A toolchain was developed to build parametric geometries and automatically generate the mesh. It is now possible to start looking at the effect of the parameters in the design space in CFD.

The isolated propeller results show variations with disk thickness large enough to justify a disk thickness study aimed at finding the sweet spot. Thrust and torque from BET line and unsteady are similar, followed by BET disk. BET disk thrust and torque are off by 10% - 25% depending on the flow condition, but the BET disk in comparison to AD captures the blade tip separation at low speed. Further work on the BET disk could improve this model.

The presence of surfaces that interact with the propeller streamtube, such as the centerbody and pylon, are shown to have significant impact on the overall force prediction. The absence of these bodies substantially alter the swirl of the propeller slipstream when it impinges on the flaps, and have a significant impact on the separation of the main-element, flap, and vane.

Skin friction coefficient and swirl comparison shows that BET disk is closer to BET line than AD but it predicts flap separation at some conditions that the BET line does not (nor the unsteady run). For the one condition we could compare, main-element  $C_L$  is higher with BET disk by 20% in comparison to BET line, while flap and vane  $C_L$  are similar. A more complete comparison would require analysis at several different operating points; the high computational cost of the unsteady and BET line methods limited the number of cases which could be run. This confirms our assumption in the abstract that the BET disk method, which adapts to the flow as shown by the  $C_{p_r}$  plots, gives results closer to the higher-fidelity tools than the AD method, at essentially equivalent computational cost.

Varying  $\alpha$  and  $T_c$  in the 3D geometry gave the same conclusions as those reached using the model problem, thus proving its utility but 3D geometry runs are still needed to get the performance reduction from the real geometry.

Further work could include an angle of attack and  $T_c$  sweep with the BET line to better understand the separation difference and how it impacts the performance at different flow conditions. Another area of interest could be cases in ground effect, as the propeller streamtube and its swirl would interact not only with the wing and high lift device but also with the ground.

## VII. Appendix

### A. Propulsion Model Description

Below is a mathematical description of the four propulsion models that will be compared.

#### 1. Actuator Disk Model

The RANS equations are coupled with the actuator disk model through a source term, i.e. a body force locally applied within the actuator disk region. The thrust per unit area is prescribed by the user, so the body force along the axial direction  $F_{ax}$  (i.e. thrust per unit volume) is given by,

$$F_{ax} = \frac{\text{Thrust per unit area}}{\text{Actuator disk thickness}} \quad (2)$$

where the actuator disk thickness is also adjustable by the user. Similarly, the circumferential force per unit volume  $F_{\text{cir}}$  can be written as,

$$F_{\text{cir}} = \frac{\text{Circumferential force per unit area}}{\text{Actuator disk thickness}} \quad (3)$$

Alternatively, the user can directly specify the targeted circumferential velocity. Consider an infinitesimally small area  $dA$  on the actuator disk. The mass flow through  $dA$  is given by,

$$dm = \rho v_{\text{ax}} dA \quad (4)$$

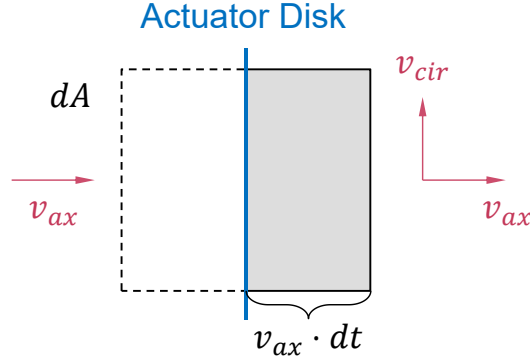


**Fig. 33 Control volume across the actuator disk.**

Along the circumferential direction, the conservation of momentum can be written as,

$$\begin{aligned} df_{\text{cir}} &= v_{\text{cir}} dm \\ &= \rho v_{\text{ax}} v_{\text{cir}} dA \end{aligned} \quad (5)$$

where  $df_{\text{cir}}$  is the circumferential force acting on the fluid within the control volume. Therefore, the circumferential force per unit area can be written as,

$$\frac{df_{\text{cir}}}{dA} = \rho v_{\text{ax}} v_{\text{cir}} \quad (6)$$

As for the output quantities, the total thrust, torque and power are defined as,

$$\begin{aligned} \text{Thrust} &= \iiint F_{\text{ax}} dV \\ \text{Torque} &= \iiint F_{\text{cir}} r dV \\ \text{Power} &= \iiint \vec{F} \cdot \vec{v} dV \end{aligned} \quad (7)$$

A realistic distribution of  $F_{\text{ax}}$  and  $F_{\text{cir}}$  is chosen to correspond to the Betz-Prandtl circulation distribution. First, using actuator-disk theory we estimate the average axial velocity through the propeller disk from its thrust disk loading and the freestream velocity.

$$v_{\text{ax}} = \frac{1}{2} \left[ \sqrt{\frac{2T}{\rho\pi R^2} + v_{\infty}^2} + v_{\infty} \right] \quad (8)$$

This then defines an effective wake advance ratio of the helical vortex sheets deposited by the blades.

$$\lambda_w = \frac{v_{\text{ax}}}{\Omega R} \quad (9)$$

The Betz-Prandtl circulation distribution which approximately minimizes the induced losses is then

$$\begin{aligned}
\Gamma(r) &= K \Gamma_1 \\
\Gamma_1(r) &= \frac{F \xi^2}{\lambda_w^2 + \xi^2} \\
\xi(r) &= \frac{r}{R} \\
F(r) &= \frac{2}{\pi} \arccos(e^{-f}) \\
f(r) &= \frac{B}{2} (1 - \xi) \sqrt{1 + 1/\lambda_w^2}
\end{aligned} \tag{10}$$

where  $F$  is the Prandtl tip-loss factor and  $B$  is the number of blades. The scaling constant  $K$  is determined to obtain the specified propeller thrust  $T$ . This is computed by numerically integrating the Kutta-Joukowski relation along the blade.

$$\begin{aligned}
T_1 &= B \int_0^R \rho \Omega r \Gamma_1 dr \\
K &= \frac{T}{T_1}
\end{aligned} \tag{11}$$

Finally, we get the local axial force (thrust) per area and also the local circumferential force per area, which are used to determine the volume body forces for the RANS calculation.

$$\begin{aligned}
f_{\text{ax}} &= \frac{\rho \Omega r \Gamma}{2\pi r} \\
f_{\text{cir}} &= \frac{\rho v_{\text{ax}} \Gamma}{2\pi r}
\end{aligned} \tag{12}$$

## 2. Blade Element Model

The RANS equations are coupled with the Blade Element Theory through a source term applied to the Navier-Stokes equations. The fictitious blades produce a force on the flow field according to the velocity the local airfoil section observes. Each blade section is treated as a two-dimensional airfoil. The blade rotational speed, twist distribution, chord distribution, and sectional airfoil polars are used to compute the  $c_d$  and  $c_l$  at every location along the blade based on the local flow velocity. These lift and drag coefficients prescribe a forcing term to the momentum components of the Navier-Stokes equation. The flowfield then evolves, and an updated velocity field is fed back into the BET model and this process continues until nonlinear convergence is reached.

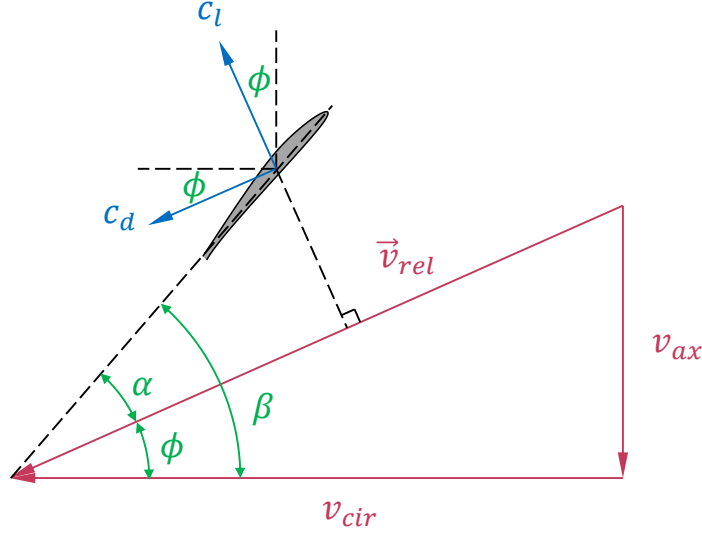


**Fig. 34 Schematic of BET for an blade airfoil section**

The local disk flow angle  $\phi$  can be computed as

$$\phi = \text{atan2}(v_{ax}, v_{cir}) \quad (13)$$

and the angle of attack is evaluated as according to Fig. 34

$$\alpha = \beta - \phi \quad (14)$$

The lift and drag coefficients,  $c_l$  and  $c_d$  are obtained through linear interpolation of airfoil polar lookup tables. Currently, Flow360 performs a four-dimensional interpolation across radial location  $r$ , Mach number, Reynolds number, and angle of attack to obtain the sectional coefficients.

$$\begin{aligned} c_l &= c_l(r, M, Re, \alpha) \\ c_d &= c_d(r, M, Re, \alpha) \end{aligned} \quad (15)$$

Once the sectional lift and drag coefficients are evaluated, the axial and circumferential sectional coefficients acting on the blade are computed as:

$$\begin{aligned} c_{f,ax} &= c_l \cos(\phi) - c_d \sin(\phi) && \text{Pointing up in Fig. 34} \\ c_{f,cir} &= c_l \sin(\phi) + c_d \cos(\phi) && \text{Pointing left in Fig. 34} \end{aligned} \quad (16)$$

Based on the forces acting on the blade, we can get the forces acting on the fluid and then add a source term (volume force) in the solver accordingly.

It has been determined that the standard tip loss factor used in the Blade-Element momentum theory is not well-suited to coupled BET-CFD applications, because the CFD solver will predict vortex tip roll-up. An alternative tip loss factor is suggested below:

$$\begin{aligned} \kappa &= \frac{1}{c_{tl}}(1 - r/R) \\ F(r) &= \frac{\kappa}{1 + \kappa^2} \end{aligned} \quad (17)$$

where  $c_{tl}$  is the tip loss chord ratio, set to 0.05 in all results presented. The axial and circumferential forces at each node within the BET disk can now be evaluated as:

$$\begin{aligned} F_{ax} &= \frac{F}{2t} \rho \|\mathbf{v}_{rel}\|^2 \sigma c_{f,ax} \\ F_{cir} &= \frac{F}{2t} \rho \|\mathbf{v}_{rel}\|^2 \sigma c_{f,cir} \end{aligned} \quad (18)$$

The local solidity  $\sigma$  depends on the type of analysis run. For the BET-Disk formulation, local solidity is defined as:

$$\sigma = \frac{N_b c}{2\pi r} \quad (19)$$

whereas for the BET line formulation the local solidity is defined as:

$$\sigma = \frac{2c}{c_{bl}} \cos(\pi d/c_{bl}) \quad (20)$$

where  $d$  is the distance from a disk mesh node to the closest fictitious blade. This weighting function provides a smooth distribution across the blade.

$F_{ax}$  and  $F_{cir}$  are applied to the momentum components of the Navier-Stokes equations as forcing terms.

### 3. Time-Resolved Unsteady Simulation/Full Propeller

Delayed Detached Eddy Simulation (DDES) with Spalart–Allmaras (SA) turbulence model were used. To capture the rotation motion of the propeller a rotational interface technique was used. The detailed geometry of the rotor was enclosed in a cylindrical volume where Navier-Stokes equations are solved in a rotational reference frame. The cylindrical volume is confined in a larger, stationary mesh. During simulation, the cylinder with the rotor rotates and its sides slide on the stationary mesh counterparts. Mesh nodes located on the sliding faces (sliding interface) lay on perfect circles with respect to the axis of rotation, see Fig. 35. During simulation, data is communicated on the interface. At any moment during the rotation, every single node on the rotating mesh interface (receiver node) detects its two closest nodes on the stationary mesh (donor nodes). The receiver node's solution is linearly interpolated from the solutions of the two donor nodes. The communication in reversed direction (from rotating mesh to stationary mesh) is done similarly.

Time step size is chosen such that during one time step the rotor rotates by 3 deg. The unsteady simulations were performed for 4200 time steps (full 3D geometry) to 4800 (2D model problem) which corresponds to 35 to 40 revolutions, respectively.

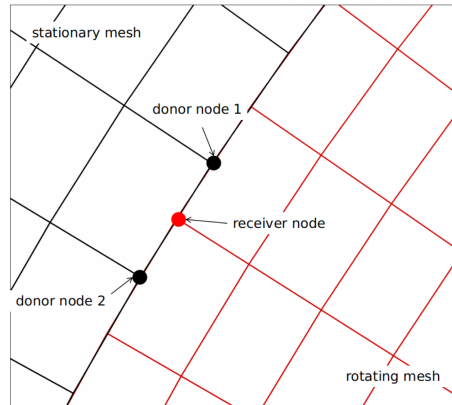


**Fig. 35 Rotational interface communication from stationary mesh to rotating mesh on a sliding interface.**

## B. Mesh Refinement

### 1. Grid Density Study for Isolated Propeller

Figure 36 shows the different refined regions. The green region immediately at the propeller is refined anisotropically by changing the number of cells in all three directions. Four yellow regions including the propeller disk and the

centerbody are refined by changing the spacing. The meshing parameters are summarized in Tab. 8 for the actuator disk model and Tab. 9 for the BET models .

If we want to double the total number of nodes in the volume mesh, then the number of nodes on the surface mesh should be roughly  $2^{2/3}$  times as the original surface mesh. Similarly, the number of nodes along the edges should be approximately  $2^{1/3}$  times as the original edges, which indicate the spacing should be around  $0.5^{1/3}$  times of the original spacing.

When doing the mesh refinement study, we can also adjust the growth rate  $r$  to change the number of anisotropic layers  $n$ .

$$\text{First layer thickness} \cdot r^n = \text{Isotropic edge length} \quad (21)$$

If we want to increase the number of layers from  $n_1$  to  $n_2$ , while keeping the first layer thickness and the isotropic edge length unchanged, then we will have:

$$\begin{aligned} r_1^{n_1} &= r_2^{n_2} \\ n_1 \cdot \ln(r_1) &= n_2 \cdot \ln(r_2) \\ n_1(r_1 - 1) &= n_2(r_2 - 1) \end{aligned} \quad (22)$$

where we assume  $r$  is close to 1 and hence we will have  $\ln(1 + \epsilon) \sim \epsilon$  as long as  $\epsilon$  is relatively small.

For example the growth rate for the medium mesh is  $r_m = 1.2$ , then for the fine mesh,

$$\begin{aligned} \frac{r_f - 1}{r_m - 1} &= \frac{n_m}{n_f} = 0.5^{1/3} \\ r_f &= 1 + 0.5^{1/3}(r_m - 1) \\ r_f &\sim 1.16 \end{aligned} \quad (23)$$

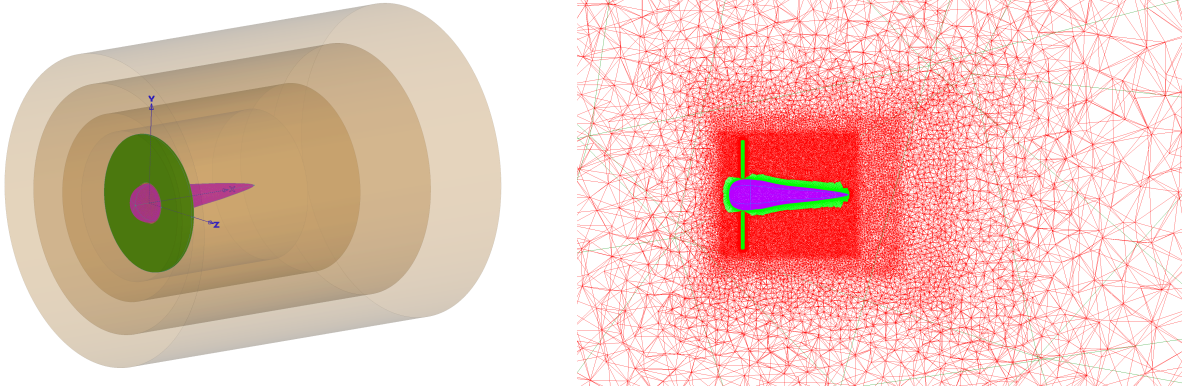


**Fig. 36** Left: Example mesh setup for isolated actuator disk, BET disk or BET line. The green washer-shaped region will be anisotropically refined, while the volume mesh in the 4 yellow cylinders will be isotropically refined with different spacings. Right: slice of volume mesh at  $y = 0$ , disk thickness is  $4\% R$ .



**Table 8 Grid density study for actuator disk. Within these meshes, the disk thickness of the anisotropic refinement region is 4%  $R$ , while the disk thickness of the region with extra body force is 1%  $R$ . Therefore the region with extra body force is fully enveloped by the anisotropic refinement region.**

	Resolution	Coarse	Medium	Fine	Extra fine
	Total number of nodes	6.09M	13.7M	24.4M	46.4M
Surface	Max edge length	12	9	7.5	5
	Curvature resolution angle	15	12	10	8
Volume	Spacing in refinement region 1	24	18	15	10
	Spacing in refinement region 2	48	36	30	20
	Spacing in refinement region 3	96	72	60	40
	Spacing in refinement region 4	192	144	120	80
	Disk thickness in % of $R$	4%	4%	4%	4%
	$n_{Cell_{thickness}}$	30	40	50	60
	$n_{Cell_{radial}}$	160	200	240	320
	$n_{Cell_{circumferential}}$	600	1000	1200	1600
	Growth rate	1.25	1.2	1.16	1.13

**Table 9 Grid density study for BET model. Within these meshes, the disk thickness of the anisotropic refinement region is 27%  $R$ , while the disk thickness of the region with extra body force is 13.5%  $R$ .**

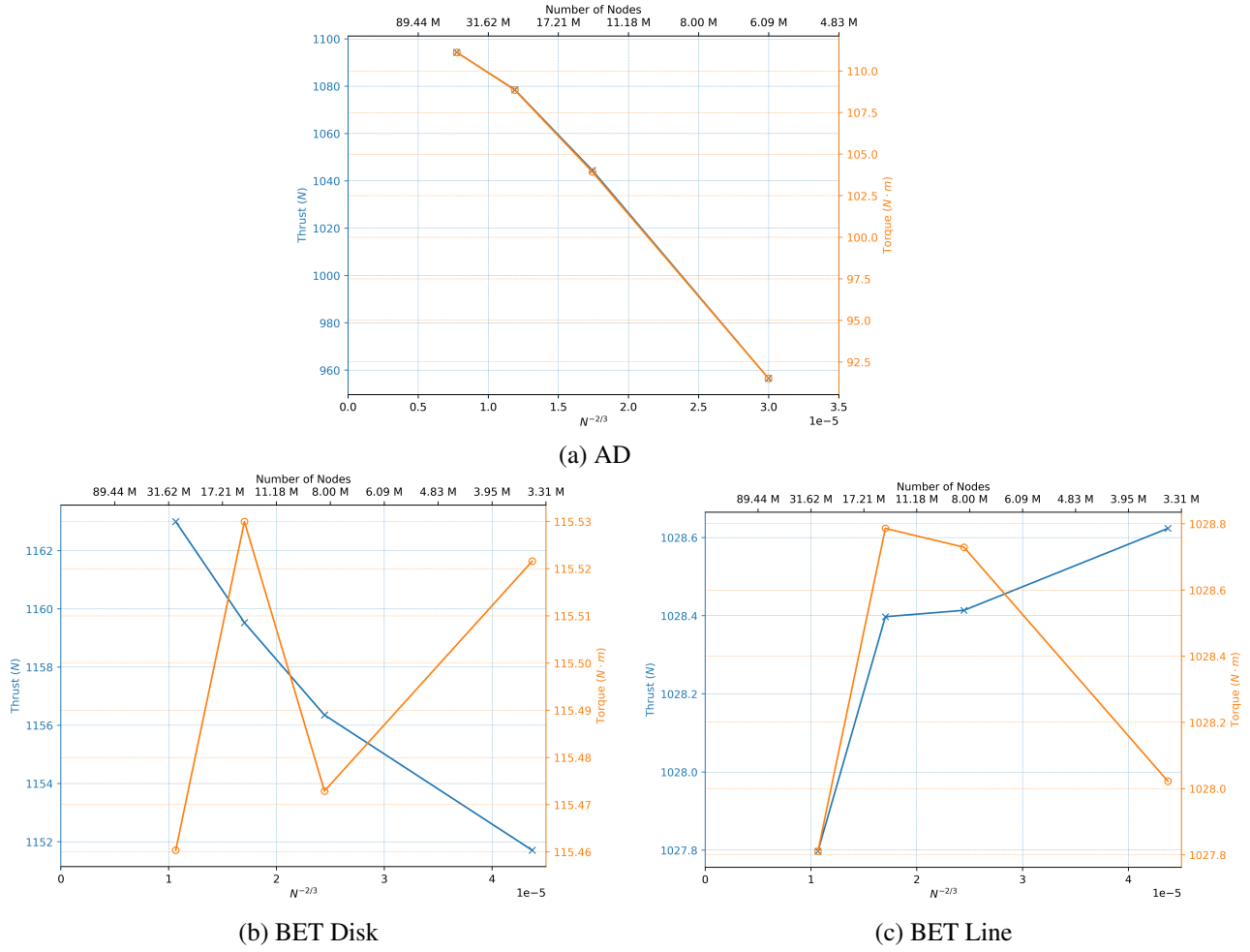
	Resolution	Coarse	Medium	Fine	Extra fine
	Total number of nodes	3.5M	8.3M	14.2M	28.7M
Surface	Max edge length	12	9	7.5	5
	Curvature resolution angle	15	12	10	8
Volume	Spacing in refinement region 1	24	18	15	10
	Spacing in refinement region 2	48	36	30	20
	Spacing in refinement region 3	96	72	60	40
	Spacing in refinement region 4	192	144	120	80
	Disk thickness in % of $R$	27%	27%	27%	27%
	$n_{Cell_{thickness}}$	30	40	50	60
	$n_{Cell_{radial}}$	160	200	240	320
	$n_{Cell_{circumferential}}$	600	1000	1200	1600
	Growth rate	1.25	1.2	1.16	1.13

It can be seen in Fig. 37, (a) that most of the thrust and torque change happens from the coarse mesh to the medium mesh for the actuator disk. The change in thrust and torque for the BET grid density study is minimal.

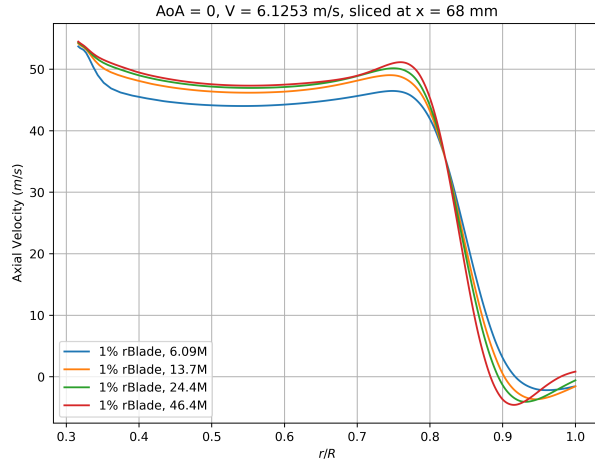
The AD sensitivities are attributed to the disk thickness being too small, if we kept the same disk thickness and run the BET models, the cases would not converge, that is why for the BET grid density study, the volume disk thickness was increased for 4 to 27%  $R$  and the solver disk thickness was increased from 1 to 13.5%  $R$ . A disk thickness study was performed in the next section to evaluate this impact.

Figure 38 (a), and (b) shows that there is almost no effect in axial velocity and swirl versus blade station for the medium to extra fine meshes. Coarse mesh underpredicts axial velocity and swirl. In (c), and (d) a comparison between BET disk and unsteady runs is made, axial velocity matches well across all meshes, there is a difference in the magnitude of the increase in swirl but the BET disk predict the increase. In (e), and (f) no difference is observed across the meshes, BET line predicts smaller magnitude of axial velocity and swirl in comparison to BET disk (this could be tentatively explained by the fact that the BET line and the full-blade models introduce effective turbulence in the rotor's streamtube) but the increase in swirl is captured at the same  $r/R$  station than the unsteady.

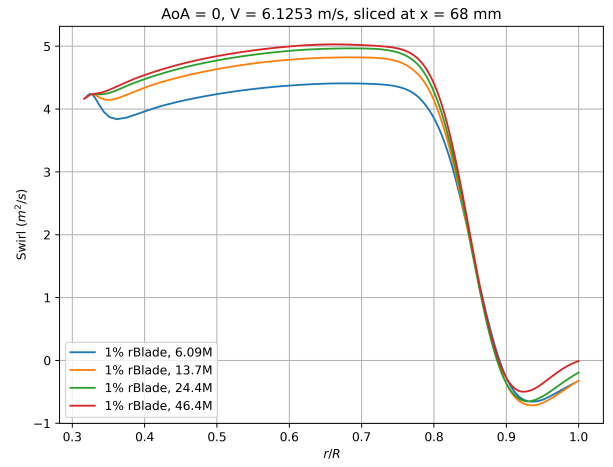
The next section shows a disk thickness study where the medium mesh for both the AD and BEM grid density study was taken and the solver disk thickness was varied.



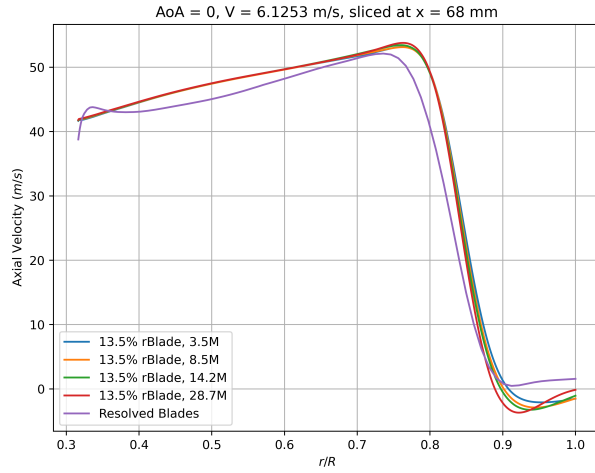
**Fig. 37 Thrust (a), torque (b), and power (c) variation with grid density for the different propulsion models.**



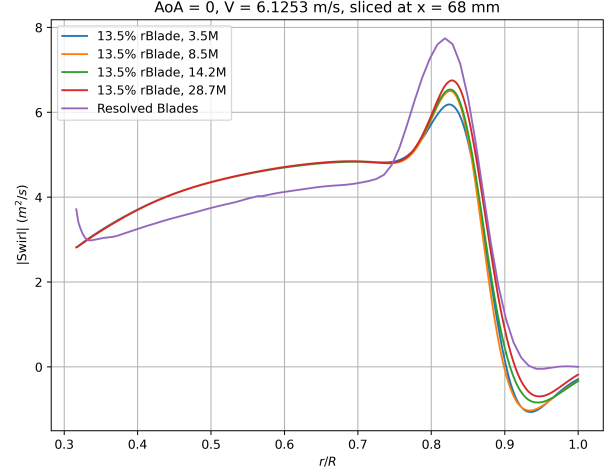
(a) AD, Axial Velocity



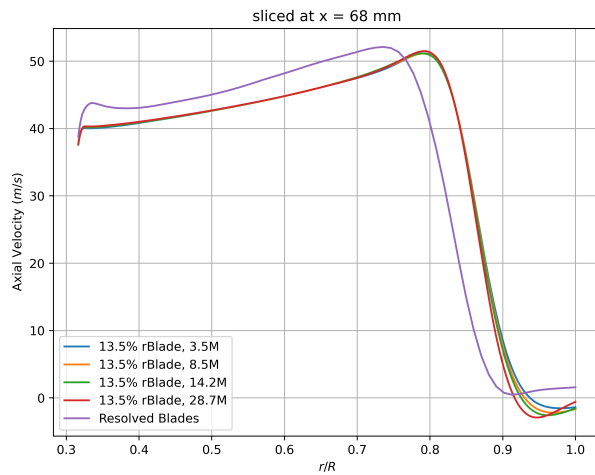
(b) AD, Swirl



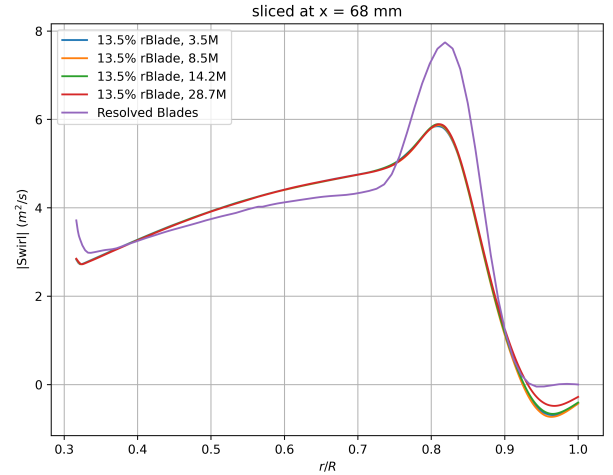
(c) BET Disk, Axial Velocity



(d) BET Disk, Swirl



(e) BET Line, Axial Velocity



(f) BET Line, Swirl

**Fig. 38 Comparison of the downstream wake with different grid density for V=6.12 m/s. (a) Disk thickness of 1% R used for the actuator disk. (b) Disk thickness of 13.5% R used for the BET disk, and (c) BET line.**

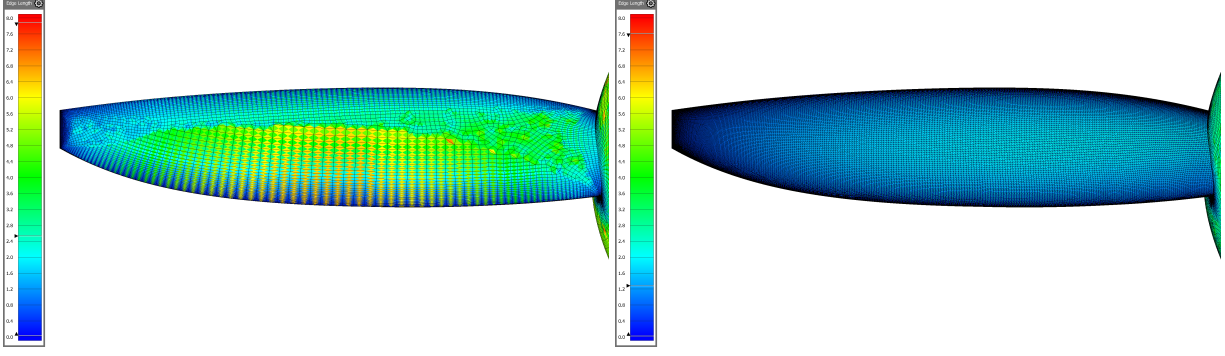


**Fig. 39** Edge length on the blades for the time-resolved unsteady simulation. Left: coarse mesh with 18M nodes in total. Right: Fine mesh with 40M in total.

**Time-Resolved Unsteady Simulation** As shown in figure 39 and table 10, when refining the mesh, instead of uniformly increasing the grid density, we intentionally distribute more nodes on the blades/spinner and in the rotational nearfield block to ensure the flow field near the rotor is well resolved and hence we can accurately predict the thrust and torque acting on the rotor. The results show that the thrust, torque and power variation between the coarse and fine meshes is minimal so the coarse mesh was chosen to run the angle of attack and Mach number sweep.

**Table 10** Grid density study for Time-Resolved Unsteady Simulation. Thrust, torque and power averaged over last 5 revolutions.

	Resolution	Coarse	Fine
Surface	Number of nodes on surface mesh	117.3K	364.5K
	Blade (each)	15.9K	61.7K
	Spinner	15.9K	34K
	Fairing	22.8K	22.8K
Volume	Number of nodes in volume mesh	18.9M	40M
	Rotational block	11.45M	31.83M
	Far-field block	7.46M	9.47M
Results	Thrust (N)	938.36	934.60
	Torque (N·m)	102.29	101.70
	Power (kW)	42.85	42.60

## 2. Grid Density Study for Model Problem

A grid density study was performed for the BET models and the disk thickness was used from the isolated propeller study, the meshing parameters are found in Tab. 11. The chosen grid was used for the other propulsion model.

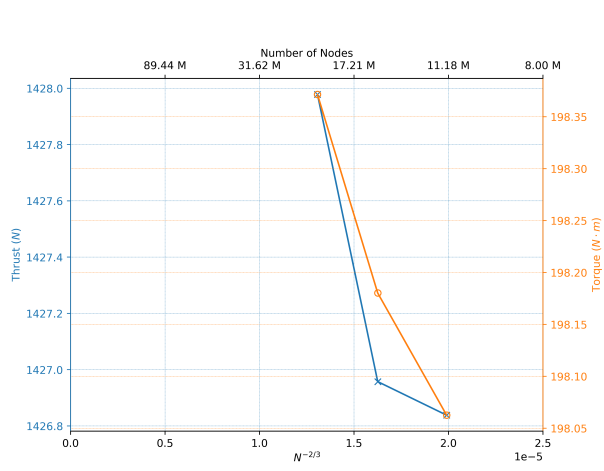
**Table 11 Grid Density Study for the Model-problem.**

	Resolution	Coarse	Medium	Fine
	Total number of nodes	12.2M	16.3M	22.3M
Surface	Max edge length	20	16	13
	Centerbody, pylon, vane	12	9	7.5
	Flap	15	12	10
	Curvature resolution angle	15	12	10
	2D anisotropic layer growth rate	1.25	1.2	1.16
Volume	Spacing in the box refinement region	24	18	15
	3D anisotropic layer growth rate	1.25	1.2	1.16

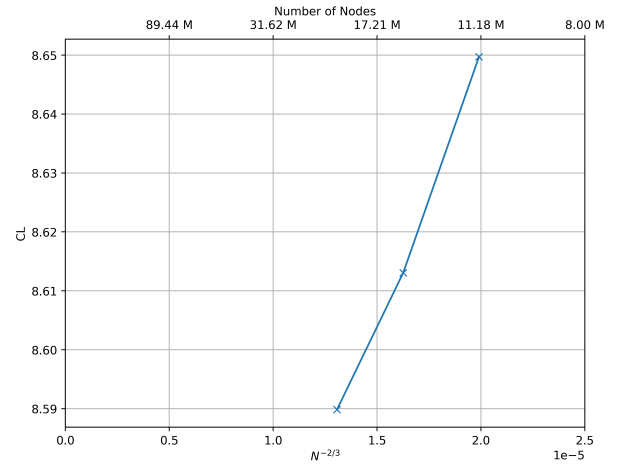
The grid resolution was done on  $\alpha = 15$  deg,  $T_c = 2$ , that corresponds to the highest  $\alpha$  that was run.

Thrust and torque variation with the grid density is negligible as seen in Fig. 40, (a). Similarly, plots (b), (c) and (d) show that there is less than 1% change in  $C_L$ ,  $C_D$ , and  $C_M$ . The coarser grid was chosen.

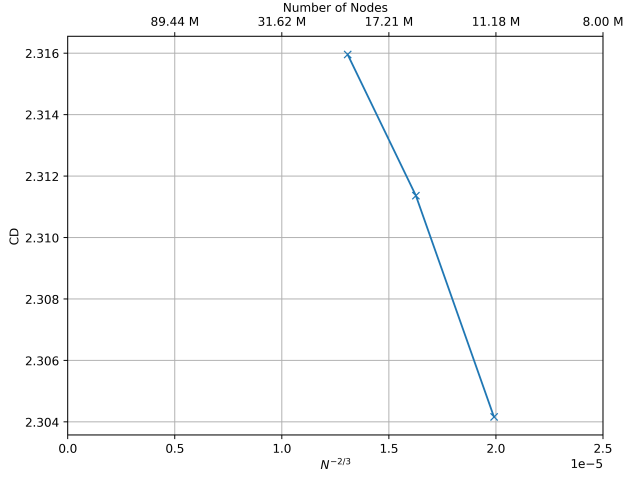
As shown in figure 41, the radius the the farfield "ring" is set as 30 times of the diagonal of the bounding box enclosing the geometry, to ensure the farfield boundary is far away from the geometry.



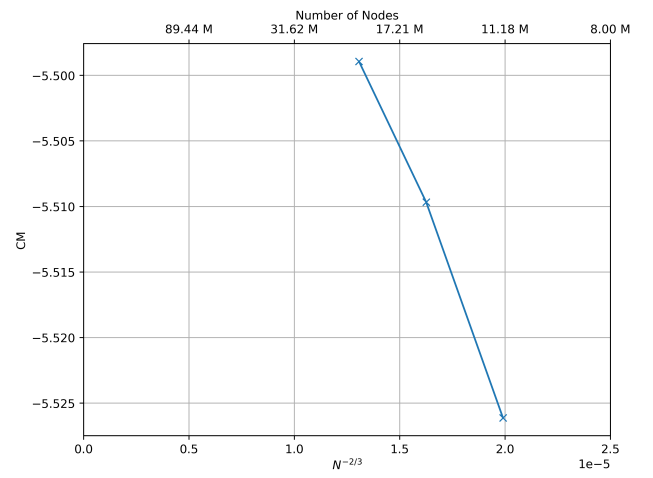
(a) Thrust and Torque



(b) Total  $C_L$



(c) Total  $C_D$



(d) Total  $C_M$

**Fig. 40** Grid convergence of rotor thrust/torque and solid body  $C_L$ ,  $C_D$ ,  $C_M$  for the 2D model rotor problem.

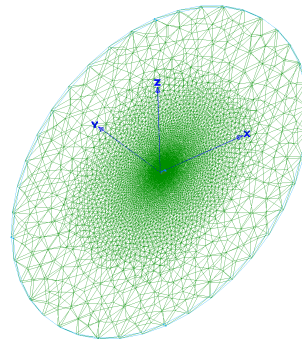
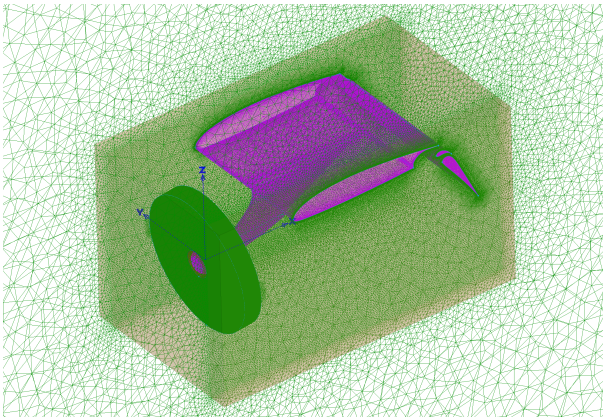


**Fig. 41** Mesh for the model problem. Left: Zoom-in. Right: Zoom-out.

### VIII. $C_{p_t}$ Definition

It is well known that:

$$\frac{p_t}{p} = \left(1 + \frac{\gamma-1}{2} M^2\right)^{\frac{\gamma}{\gamma-1}} \quad \text{and} \quad \frac{p_{t\infty}}{p_\infty} = \left(1 + \frac{\gamma-1}{2} M_\infty^2\right)^{\frac{\gamma}{\gamma-1}} \quad (24)$$

$$q_\infty = \frac{1}{2} \rho_\infty U_\infty^2 = \frac{\gamma}{2} p_\infty M_\infty^2 \quad (25)$$

The pressure coefficient can be written as:

$$\begin{aligned} C_{p_t} &= \frac{p_t - p_{t\infty}}{q_\infty} \\ &= \frac{p \left(1 + \frac{\gamma-1}{2} M^2\right)^{\frac{\gamma}{\gamma-1}} - p_\infty \left(1 + \frac{\gamma-1}{2} M_\infty^2\right)^{\frac{\gamma}{\gamma-1}}}{\frac{\gamma}{2} p_\infty M_\infty^2} \\ &= \frac{\frac{p}{p_\infty} \left(1 + \frac{\gamma-1}{2} M^2\right)^{\frac{\gamma}{\gamma-1}} - \left(1 + \frac{\gamma-1}{2} M_\infty^2\right)^{\frac{\gamma}{\gamma-1}}}{\frac{\gamma}{2} M_\infty^2} \end{aligned} \quad (26)$$

Note that the non-dimensional pressure  $p_{\text{non-dim}}$  can be written as,

$$p_{\text{non-dim}} = \frac{p}{\rho_\infty C_\infty^2} \quad (27)$$

where  $C_\infty$  is the free-stream speed of sound,

$$C_\infty = \sqrt{\gamma \frac{p_\infty}{\rho_\infty}} \quad (28)$$

Therefore,

$$\frac{p}{p_\infty} = \frac{\rho_\infty C_\infty^2}{p_\infty} p_{\text{non-dim}} = \gamma p_{\text{non-dim}} \quad (29)$$

All terms in eq. 26 are output from the CFD solver and  $C_{p_t}$  can be computed. Warm colors mean energy is added to the flow while cold colors mean losses.

### Acknowledgments

We are very grateful to John Moore for assistance and valuable discussion on the blade element method. We also thank Matthew Berk, project engineer at Electra.aero, who helped setup the ESP model.

### References

- [1] Van Kuik, G., *The fluid dynamic basis for actuator disc and rotor theories*, IOS Press, 2018.
- [2] Spalart, P. R., "On the simple actuator disk," *Journal of fluid mechanics*, Vol. 494, 2003, pp. 399–405.
- [3] Field, M., "A Conservative , Scalable , Space-Time Blade Element Rotor Model for Multirotor Vehicles," 2018.
- [4] Uwatoko, K., Kanazaki, M., Nagai, H., Fujita, K., and Oyama, A., "Blade Element Theory Coupled with CFD Applied to Optimal Design of Rotor for Mars Exploration Helicopter," 2020. <https://doi.org/10.2514/6.2020-1284>.
- [5] Halwick, J., "Implementation of Blade Element Theory in CFD Analysis of Edgewise Ducted Fan Vehicles," Master's thesis, Pennsylvania State University, 2012.
- [6] Mentey, J., "Time Dependent Actuator Model for a Helicopter Rotor in Hover," Master's thesis, Pennsylvania State University, 2012.
- [7] Haimes, R., and Dannenhoffer, J. F., "The Engineering Sketch Pad: A Solid-Modeling, Feature-Based, Web-Enabled System for Building Parametric Geometry," 2013.
- [8] Drela, M., and Youngren, H., "XROTOR: design and analysis of ducted and free-tip propellers and windmills <http://web.mit.edu/drela/Public/web/xrotor/>," 1998.